

Vegetation Index Weighted Canopy Volume Model (CVM_{VI}) for soybean biomass estimation from Unmanned Aerial System-based RGB imagery



Maitiniyazi Maimaitijiang^a, Vasit Sagan^{a,*}, Paheding Sidike^a, Matthew Maimaitiyiming^a, Sean Hartling^a, Kyle T. Peterson^a, Michael J.W. Maw^{b,d}, Nadia Shakoor^c, Todd Mockler^c, Felix B. Fritsch^d

^a Department of Earth and Atmospheric Sciences, Saint Louis University, St. Louis, MO 63108, USA

^b School of Agriculture & Natural Resources, Abraham Baldwin Agricultural College, Tifton, GA 31793, USA

^c Donald Danforth Plant Science Center, St. Louis, MO 63132, USA

^d Division of Plant Sciences, University of Missouri, Columbia, MO 65211, USA

ARTICLE INFO

Keywords:

Canopy volume model (CVM)
Vegetation index weighted canopy volume model (CVM_{VI})
Unmanned Aerial Systems (UAS)
Biomass estimation
Photogrammetric point clouds

ABSTRACT

Crop biomass estimation with high accuracy at low-cost is valuable for precision agriculture and high-throughput phenotyping. Recent technological advances in Unmanned Aerial Systems (UAS) significantly facilitate data acquisition at low-cost along with high spatial, spectral, and temporal resolution. The objective of this study was to explore the potential of UAS RGB imagery-derived spectral, structural, and volumetric information, as well as a proposed vegetation index weighted canopy volume model (CVM_{VI}) for soybean [*Glycine max* (L.) Merr.] aboveground biomass (AGB) estimation. RGB images were collected from low-cost UAS throughout the growing season at a field site near Columbia, Missouri, USA. High-density point clouds were produced using the structure from motion (SfM) technique through a photogrammetric workflow based on UAS stereo images. Two-dimensional (2D) canopy structure metrics such as canopy height (CH) and canopy projected basal area (BA), as well as three-dimensional (3D) volumetric metrics such as canopy volume model (CVM) were derived from photogrammetric point clouds. A variety of vegetation indices (VIs) were also extracted from RGB orthomosaics. Then, CVM_{VI} , which combines canopy spectral and volumetric information, was proposed. Commonly used regression models were established based on the UAS-derived information and field-measured AGB with a leave-one-out cross-validation. The results show that: (1) In general, canopy 2D structural metrics CH and BA yielded higher correlation with AGB than VIs. (2) Three-dimensional metrics, such as CVM, that encompass both horizontal and vertical properties of canopy provided better estimates for AGB compared to 2D structural metrics ($R^2 = 0.849$; RRMSE = 18.7%; MPSE = 20.8%). (3) Optimized CVM_{VI} , which incorporates both canopy spectral and 3D volumetric information outperformed the other indices and metrics, and was a better predictor for AGB estimation ($R^2 = 0.893$; RRMSE = 16.3%; MPSE = 19.5%). In addition, CVM_{VI} showed equal prediction power for different genotypes, which indicates its potential for high-throughput soybean biomass estimation. Moreover, a CVM_{VI} based univariate regression model yielded AGB predicting capability comparable to multivariate complex regression models such as stepwise multilinear regression (SMR) and partial least squares regression (PLSR) that incorporate multiple canopy spectral indices and structural metrics. Overall, this study reveals the potential of canopy spectral, structural and volumetric information, and their combination (i.e., CVM_{VI}) for estimations of soybean AGB. CVM_{VI} was shown to be simple but effective in estimating AGB, and could be applied for high-throughput phenotyping and precision agro-ecological applications and management.

1. Introduction

Aboveground biomass (AGB) of crops is a basic agro-ecological indicator to assess the responses of plants to environmental conditions

and management practices, and for precision agriculture and plant phenotyping (Araus and Cairns, 2014; Busemeyer et al., 2013; Lati et al., 2013b). It reflects the status of crop growth and is related to light use efficiency, as well as yield and grain quality (Donald, 2006;

* Corresponding author.

E-mail address: vasit.sagan@slu.edu (V. Sagan).

Hensgen et al., 2016). AGB of crops may also indicate the physiological condition of a plant, and, as such, can influence management decisions related to fertilizer application and pest control (Avolio et al., 2018; Lati et al., 2013a). Thus, rapid, accurate and economical estimation of crop AGB during the growing season is valuable for crop growth monitoring and yield estimation, risk management and decision-making (Becker-Reshef et al., 2010; Li et al., 2015a).

Traditionally, crop biomass is measured by harvesting, drying, and weighing of plant samples, which is accurate but destructive, labor-intensive, time-consuming and not operationally feasible for large-scale spatial and temporal measurements (Wang et al., 2017). Thus, destructive methods are impractical particularly for next-generation field-based high-throughput phenotyping (Walter et al., 2018).

As an alternative, remote sensing based-methods have gained importance for estimation of vegetation biomass due to their ability to collect multi-temporal information at local, regional and global scales at a relatively low-cost (Claverie et al., 2012; Ene et al., 2018). Spectral information acquired from different remote sensing platforms (spaceborne, airborne, UAS and ground-based platforms) and sensors such as multispectral and hyperspectral have been employed for crop biomass estimation in many recent studies (Avitabile et al., 2012; Claverie et al., 2012; Marshall and Thenkabail, 2015). However, due to the asymptotic spectral saturation problem along with limited canopy three-dimensional (3D) structure information captured by multispectral or hyperspectral sensors, it is difficult to distinguish biomass of plants with various heights, high density (Greaves et al., 2015; Selkowitz, 2010), or significant spatial heterogeneity (Luo et al., 2017; Wang et al., 2017). Moreover, spectral information derived from coarse and moderate spatial resolution optical remote sensing images is often impacted by plant canopy architecture, background soil, etc., which complicates the ability to identify and quantify low-stature vegetation especially with heterogeneous spatial distribution (Greaves et al., 2016).

Light Detection and Ranging (LiDAR) technique, which is capable of providing 3D information on vegetation canopy structure, is less prone to saturation effects and can discriminate subtle changes in plant height and density (Clark et al., 2011; Greaves et al., 2015; Swatantran et al., 2011). Both airborne laser scanning (ALS) and terrestrial laser scanning (TLS) LiDAR systems have been widely used in tree and shrub biomass estimation for determining canopy structural and volumetric attributes such as vegetation height, coverage, tree crown size, and canopy volume, etc. at relatively fine scales (Gonzalez de Tanago et al., 2017; Greaves et al., 2015; Kim et al., 2016; Stovall et al., 2017). Additionally, fusion of canopy structure information from LiDAR and spectral information from multispectral/hyperspectral sensors has been reported to be a highly accurate method for biomass estimation (Greaves et al., 2016; Li et al., 2015b; Luo et al., 2017; Wang et al., 2017). However, very few studies have been conducted to estimate biomass of low-stature plants such as crops using canopy 3D structure information from LiDAR (Wang et al., 2017). This may be due to the inherent challenges of LiDAR systems, especially airborne LiDAR application for low-stature vegetation which requires higher density point clouds. In addition, the relatively high cost of LiDAR systems may also hinder its applications (Dandois and Ellis, 2013; Erdody and Moskal, 2010; Jayathunga et al., 2018). Particularly for high-throughput phenotyping, implementation of LiDAR systems is hampered by the complexity of data collection and processing pipelines (Verma et al., 2016; Walter et al., 2018).

Recent advances in UAS technology facilitate low-cost data collection with high spatial, spectral, and temporal resolution. UAS have become important cost-effective, high versatility and high-throughput phenotyping platforms (Jin et al., 2017; Maimaitijiang et al., 2017; Sagan et al., 2019; Yang et al., 2017). Furthermore, the development of digital photogrammetric techniques, multi-view stereopsis and computer vision algorithms such as Structure from Motion (SfM), that allow reconstructing 3D point clouds from overlapping 2D photographs, have broadened the horizons of UAS-based remote sensing (Jayathunga et al., 2018; Kalacska et al., 2017). Automated photogrammetric

systems based on SfM algorithms match image feature points using overlapped photographs acquired from multiple angles/positions and produce geometrically precise 3D point clouds (Dandois and Ellis, 2013). Despite the limited penetration capability compared to ALS (Balenovic et al., 2017; Kachamba et al., 2017), UAS and digital photogrammetric techniques are emerging as cost-effective tools (Jayathunga et al., 2018; Nurminen et al., 2013; Rahlf et al., 2014; Verma et al., 2016) that can produce point clouds at sub-pixel accuracy in near real-time with similar quality and accuracy to ALS, and even higher point density than ALS and TLS (Kalacska et al., 2017; Leberl et al., 2010; Li et al., 2016; White et al., 2013). Moreover, advancements in computer vision algorithms, such as Scale Invariant Feature Transform (Lowe, 1999), and parallel bundle adjustments on Graphics Processing Units have further improved image feature matching accuracies (Leberl et al., 2010; Rahlf et al., 2014) and consequently produce dense and highly accurate point clouds from UAS imagery (Jayathunga et al., 2018; Torresan et al., 2017).

Three-dimensional canopy structure information derived from UAS-based photogrammetric point clouds have been successfully applied in forest inventory and tree biomass estimation (Patrick and Li, 2017; Puliti et al., 2015; Wallace et al., 2017). In addition, photogrammetric point clouds-based structure information such as canopy height (CH) and the combination of CH with spectral information have been used for crop biomass estimation (Bendig et al., 2014; Bendig et al., 2015; Li et al., 2016; Maimaitijiang et al., 2017).

Aboveground biomass is a complex plant trait that is 3D in nature (Walter et al., 2018). Compared to commonly used 2D canopy structure parameters such as CH, canopy area and density, a volumetric 3D model encompasses both horizontal and vertical properties of plants and is a direct and continuous method for canopy structure characterization. It is also regarded as a significant element of allometric equations for plant biomass estimation (Djomo and Chimi, 2017; Pottier and Jabot, 2017). In recent years, point cloud-derived canopy volume metrics (either from LiDAR or Photogrammetric techniques) are gaining more and more attention and have been reported as a good proxy for aboveground tree and shrub biomass (Greaves et al., 2015; Greaves et al., 2016; Olsoy et al., 2014; Stovall et al., 2017). However, there have been few reported attempts regarding the potential of canopy volume metrics for crop biomass estimation (Eitel et al., 2014; Walter et al., 2018).

One of the key objectives of the present study was to investigate the potential of low-cost and consumer-grade platforms, as well as digital cameras for soybean [*Glycine max* (L.) Merr.] biomass estimation in the context of high-throughput field phenotyping. To this end, a variety of UAS imagery-based spectral indices, structural and volumetric metrics were derived, as well as a new model, termed vegetation index weighted canopy volume model (CVM_{VI}), was proposed. CVM_{VI} uses photogrammetric point clouds and vegetation indices (VIs) derived from ultrahigh-resolution UAS digital imagery to estimate AGB. The ability of using CVM_{VI} as a single predictor in various regression models for soybean AGB estimation was investigated. Moreover, a comparison of the proposed model with more complex models, which incorporate a variety of canopy spectral indices and structural metrics, was examined.

2. Study area and data

2.1. Test site and experimental setup

This study was carried out at the University of Missouri Bradford Research Center near Columbia, Missouri, USA (38.8N, 92.2W). Soybean was grown on a Mexico silt loam (fine, smectitic, mesic Vertic Epiaqualf) soil with a pH of 6.5. After tillage, soybean cultivars 'Pana', 'Dwight', and 'AG3432' were planted at 2.5-cm depth in rows 0.76 m apart at a density of 40 seed per m² on May 19, 2017. The field was laid out in four replications, each with irrigated and rainfed main plots and Pana, Dwight, and AG3432 as split-plots measuring 21.0 × 27.0 m or

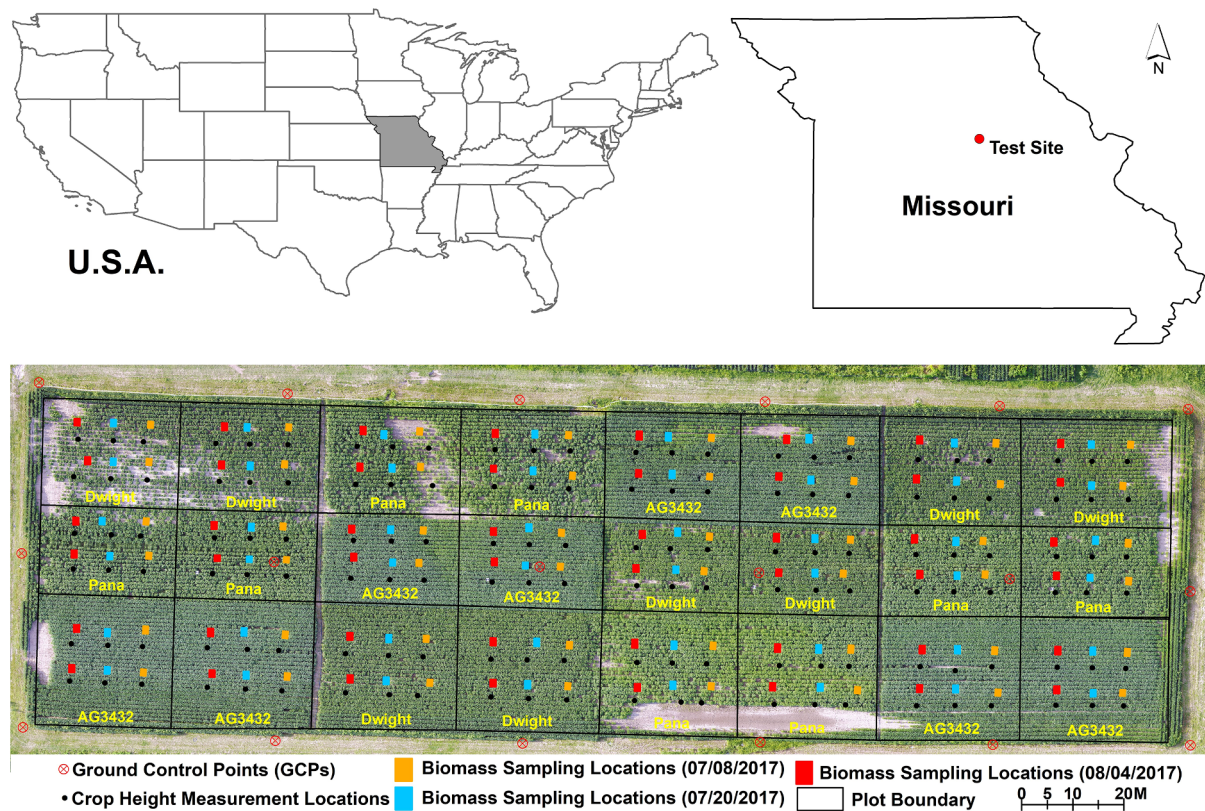


Fig. 1. Test site location. Black dots are sampling locations for canopy height; orange, blue and red rectangles represent aboveground biomass sampling locations on July 8, July 20 and August 4, respectively; circles with x are locations of Real-Time Kinematic (RTK) GPS survey Ground Control Points (GCPs). (For interpretation of the references to color in this figure legend, the reader is referred to the web version of this article.)

Table 1
Descriptive statistics of field measured parameters.

Parameters	Date	NO. of samples	Mean	Max.	Min.	SD	CV (%)
CH (m)	07/08/2017	144	0.413	0.573	0.194	0.092	22.3
	07/20/2017	144	0.587	0.801	0.326	0.103	17.5
	08/04/2017	144	0.889	1.212	0.564	0.150	16.9
	All	432	0.621	1.212	0.194	0.231	37.2
AGB (kg/m ²)	07/08/2017	48	0.468	1.170	0.097	0.244	52.1
	07/20/2017	48	1.004	1.691	0.624	0.271	27.0
	08/04/2017	48	2.132	3.324	1.193	0.445	20.9
	All	144	1.211	3.324	0.097	0.773	64.0

CH: canopy height; AGB: aboveground biomass; SD: standard deviation; CV: coefficient of variation.

17.0 × 21.0 m (Fig. 1). No fertilizers were applied and weeds were controlled by application of pre-emergence herbicide sulfentrazone at a rate of 0.3 kg ha⁻¹ and postemergence herbicide sethoxydim at a rate of 2.60 kg ha⁻¹. The climate of this region is characterized as humid continental. Temperatures, as measured by an on-farm weather station, during the growing season averaged 17.4 °C in May, 22.6 °C in June, 25.0 °C in July, 21.0 °C in August, 20.2 °C in September, and 13.8 °C in October. Monthly precipitation recorded by the same weather station was 114 mm in May, 82 mm in June, 116 mm in July, 77 mm in August, 20 mm in September, and 98 mm in October.

2.2. Data acquisition

2.2.1. Field data

Canopy height was measured at 144 locations distributed throughout the field (6 samples within each plot) (Fig. 1) on July 8, July 20 and August 4 of 2017. Each sampling location was marked with fiberglass stakes before (June 19 of 2017) the experiment for precise

ground truthing of UAS data. Instead of measuring the coordinates of the fiberglass stakes using the GPS, a more efficient method was employed: a sheet of pink paper (21.0 × 29.7 cm) was placed on each fiberglass marker such that each marker could be seen on the UAS imagery. The coordinates for the sampling locations were then extracted from the georeferenced and orthomosaicked UAS images.

In addition to ground truthing of CH, AGB samples were collected on each of the three flight dates by cutting the stems from 1 m of row length in each of two neighboring rows approximately 2 cm above the soil surface (Fig. 1). On each sampling date, AGB was collected at two locations in each plot. The fresh weight was measured immediately and samples were then oven-dried at 60.0 °C until weights stabilized. Lastly, dry samples were weighed to obtain the aboveground dry biomass which was used in this study. The statistics of field-measured plant traits are shown in Table 1.

Biomass sampling locations are often measured using survey grade high accuracy GPS systems in the field (Greaves et al., 2016; Li et al., 2015a). In this study, we propose an efficient yet accurate procedure to

identify the biomass sampling spots and boundaries by accurate georeferencing and overlapping two UAS-based orthomosaics acquired before and after biomass sampling.

2.2.2. UAS data acquisition

In conjunction with CH and AGB ground samplings, high resolution RGB imagery was simultaneously collected via UAS. Ground and UAS field campaigns were conducted from 10:30 AM through 3:00 PM local time on July 8, July 20 and August 4 of 2017, respectively. RGB color imagery was acquired using a Mapir Survey-2 RGB camera mounted on a DJI S1000 + octocopter frame. Mapir Survey-2 RGB camera employs a 16-megapixel Exmor sensor and 23-mm focal length with an 82-degree field-of-view lens. Images in this study were captured in sub-centimeter pixel resolution.

All flight systems were equipped with a 3D Robotics Pixhawk autopilot controller enabling user-defined autonomous waypoint flight operations. Flight missions were planned utilizing Mission Planner, an open source full-featured ground station application for UAS autopilot systems. All missions were planned at a flight altitude of 30 m and flight speed of 5 m/s with an intended overlap of 90% and side-lap of 90% to ensure image redundancy for post-processing such as orthomosaicking. Flight missions remained constant throughout the study period to ensure consistency in data collection. To ensure the optimal exposure and to prevent images from being affected by motion, shutter speed was changed between 1/500 s and 1/800 s, while ISO was set to 50 based on the illumination condition.

To capture biomass sampling locations, additional flights were conducted to collect images after biomass sampling using a DJI Mavic Pro quadcopter (DJI Inc., Shenzhen, China). The Mavic Pro is a small, light-weight commercial platform weighting 743 g and with a 27-minute maximum flight time. The images were geotagged automatically by its built-in satellite positioning systems (GPS/Global Navigation Satellite System). The Mavic Pro quadcopter is equipped with a small RGB camera and 3D gimbal system, and the camera employs a 12.4-Mpixel CMOS sensor and 5-mm focal length with a 78.8-degree field-of-view lens which has been successfully used for UAS image enhancement (Sidike et al., 2018).

Prior to image collection, 18 fixed Ground Control Points (GCPs) (14 plastic GCPs located around the field and 4 raised wooden GCPs located within the field) (Fig. 1) were marked and positioned in the field using a Trimble R8 GNSS Rover with access to the Missouri Statewide Real Time GNSS Network, which provides about 10 mm and 20 mm accuracy at horizontal and vertical direction, respectively.

2.3. Image preprocessing

The collection of RGB images obtained from UAS missions was loaded into Pix4Dmapper software package (Pix4D SA, Lausanne, Switzerland), which is specifically designed to process UAS data and utilizes techniques rooted in both computer vision and photogrammetry (Turner et al., 2014; Turner et al., 2012). Images were aligned based on tie points, and subsequently orthorectified and mosaicked. To improve the accuracy of the final mosaics, camera information such as sensor dimensions, principal points, pixel size, and focal length were incorporated for processing. To ensure the accuracy of scale and geometry of the resultant scene, the geographic information of 18 survey grade high accuracy GCPs was applied to the stereo images to improve the horizontal and vertical accuracy of the outputs during the photogrammetric workflow through a bundle adjustment within the software.

High-density point clouds were generated using Pix4Dmapper's SfM algorithm along with photogrammetric workflow. To build high density and accurate point clouds, "half image size" for the image scale option and "high setting" for the point density option of Pix4Dmapper software were selected, as these options are specifically recommended for targets such as vegetation. The SfM point clouds were geo-referenced

during the photogrammetric workflow by incorporating the high accuracy geographic information of the 18 GCPs. To finalize the data products, the resulting dense point cloud was exported to LAS format for subsequent processing, and all datasets were then projected to a common horizontal and vertical coordinate system (WGS 1984 UTM Zone 15N (horizontal) with the NAVD 88 vertical datum).

Atmospheric conditions, illumination intensity and sensor view geometry change over time (de Carvalh et al., 2013), thus absolute radiometric calibration or relative normalization is often employed to maintain consistency and temporal comparability in the case of multi-temporal remote sensing images (Teillet et al., 2001; Tokola et al., 1999). In this study, the pseudo-invariant features (PIF) method was applied to the orthomosaics to carry out radiometric normalization. The PIF method uses ground objects with near constant reflectance values over time as reference data for normalization (Du et al., 2002). Our study area was mainly occupied with crops, and it is challenging to select ideal PIFs due to the varying reflectance of vegetation over time. Therefore, we used color checkerboard as ground targets, and each color on the checkerboard represents one PIF. The color checkerboard covers a wide range of radiometric values and keeps near constant reflectance over time. UAS images of the color checkerboard were taken before each flight. The mean pixel value of each PIF on each date was calculated and used as independent variables of the linear radiometric normalization model. Dependent variables, or also called reference data of the model, were generated by averaging each PIF's multi-temporal pixel values of the blue, green, and red band, respectively (Du and Noguchi, 2017). Consequently, a linear radiometric normalization model of each day was applied to corresponding orthomosaics.

3. Methods

3.1. Spectral indices and structural metrics

3.1.1. Canopy spectral indices

A set of common VIs (Table 2) for biomass estimation was calculated from RGB orthomosaics, and corresponding raster layers were generated. Soil and weeds were removed from the raster layers using binary masks generated from the orthorectified RGB images (see Section 3.1.3) where Support Vector Machine (SVM) (Cortes and Vapnik, 1995) was used as a classifier. For each of these raster layers, average pixel values were calculated for each sampling spot by zonal statistics to relate them to the ground biomass measurements. The Arcpy library and Python2.7 programming language were used to automate and streamline the extraction of VIs and removal of soil/weeds.

3.1.2. Canopy structure metrics

Unlike airborne LiDAR, photogrammetric point clouds cannot provide accurate terrain elevation information of vegetated areas because of limited penetration capability; they mainly provide the height information of the upper canopy surface (White et al., 2013). Thus, to determine bare-earth elevation, UAS imagery was collected over the bare-soil field immediately after planting on May 25, 2017, and photogrammetric point clouds for bare-earth were created for the Digital Elevation Model (DEM). Soybean canopy point clouds from July 8, July 20 and August 4 of 2017 were used for Digital Surface Model (DSM) generation, respectively.

Photogrammetric point clouds for each sampling day were exported to LAS format from the Pix4DMapper software. Noise filtering was applied for high-density photogrammetric point clouds using LiDAR package of ENVI 5.4.1 software (Exelis Visual Information Solutions, Boulder, Colorado, US) to remove outliers such as points with abnormal height values. The filtered LAS dataset was then converted to raster layers using the Inverse Distance Weighting (IDW) interpolation method with a consistent spatial resolution of 0.6 cm in ArcGIS 10.4.1 software package, and a no void filling mode was used to construct more accurate models (Jayathunga et al., 2018). IDW is a deterministic,

Table 2

Definitions of the Vegetation Indices (VIs) extracted from orthorectified RGB mosaics.

Spectral indices	Definition	References
Red (R), Green (G), Blue (B)	raw value of each band	/
Normalized Red (rn), Green (gn), Blue (bn)	$rn = R/(R + G + B); gn = G/(R + G + B); bn = B/(R + G + B)$	/
Green red ratio index	GRRI = G/R	/
Green blue ratio index	GBRI = G/B	/
Red blue ratio index	RBRI = R/B	/
Color intensity index	INT = $(R + G + B)/3$	(Ahmad and Reid, 1996)
Green-red vegetation index	GRVI = $(G - R)/(G + R)$	(Tucker, 1979)
Normalized difference index	NDI = $(rn - gn)/(rn + gn + 0.01)$	(Woebbecke et al., 1992)
Woebbecke index	WI = $(G - B)/(R - G)$	(Woebbecke et al., 1995)
Kawashima index	IKAW = $(R - B)/(R + B)$	(Kawashima and Nakatani, 1998)
Green leaf index	GLI = $(2 \times G - R - B)/(2 \times G + R + B)$	(Louhaichi et al., 2001)
Visible atmospherically resistance index	VARI = $(G - R)/(G + R - B)$	(Gitelson et al., 2002)
Excess red vegetation index	ExR = $1.4 \times rn - gn$	(Mao et al., 2003)
Excess green vegetation index	ExG = $2 \times gn - rn - bn$	(Mao et al., 2003)
Excess blue vegetation index	ExB = $1.4 \times bn - gn$	(Mao et al., 2003)
Excess green minus Excess red index	ExGR = ExG - ExR	(Mao et al., 2003)
Vegetative index	VEG = $G/(R^a \times B^{(1-a)})$, $a = 0.667$	(Hague et al., 2006)
Principal component analysis index	IPCA = $0.994 \times R - B + 0.961 \times G - B + 0.914 \times G - R $	(Saberioon et al., 2014)
Color index of vegetation	CIVE = $0.441 \times R - 0.881 \times G + 0.385 \times B + 18.78745$	(Kataoka et al., 2003)
Combination	COM = $0.25 \times ExG + 0.3 \times ExGR + 0.33 \times CIVE + 0.12 \times VEG$	(Guizarro et al., 2011)

exact interpolation method, and retains a measured value at its sample location (Johnston et al., 2001). Hence, the method is suitable for preserving the accuracy of measurements with a high density (Tilly et al., 2014).

A canopy height model (CHM) for each sampling day was generated by computing the pixel-wise difference between DSM and DEM, respectively (Wallace et al., 2017; Zhao et al., 2018). Soil and weeds pixels in CHM were removed using masks created from the classification results of orthorectified RGB images (see Section 3.1.3). The accuracy of CHM was evaluated against the 432 field-measured CH samples (see Section 4.1).

Canopy structure-based metrics including mean canopy height (CH_{mean}), maximum canopy height (CH_{max}), minimum canopy height (CH_{min}), standard deviation of canopy height (CH_{std}), Coefficient of Variation of canopy height (CH_{cv}), and canopy projected basal area (BA) were extracted for each sampling spot from CHM using zonal statistics (Table 3). CH_{mean} , CH_{max} , and CH_{min} can represent the vertical distribution of CH, while CH_{std} and CH_{cv} provide insights into the vertical complexity and heterogeneity of the canopy components (Li et al., 2016).

3.1.3. Soil and weed removal

SVM (Cortes and Vapnik, 1995) classifier, based on statistical learning theory and often outperforming other classifiers (Huang and Wang, 2006; Maimaitjiang et al., 2015), was employed to identify soybean, weeds and background soil in RGB orthomosaics. Mask layers for weeds and background soil were established to exclude them from all spectral indices and structural metrics for further processing. Overall accuracy (OA) and Kappa coefficient were used as validation metrics

based on randomly selected 10,000 independent testing samples to evaluate the performance of SVM classifier. The classification results showed that OA for each sampling day was higher than 99.0% and Kappa coefficient was higher than 0.990.

3.2. CVM and vegetation index weighted CVM (CVM_{Vi})

Voxel-based (voxelization) methods that convert structured point clouds to cubes (Kim et al., 2016; Stovall et al., 2017; Wallace et al., 2017), and cylinder-fitting methods, which model canopy 3D profile with a best-fit cylindrical shape from LiDAR/photogrammetric point clouds have been applied for tree/shrub volume extraction (Greaves et al., 2015; Patrick and Li, 2017). Due to the limited penetration ability of photogrammetric point clouds, upper canopy exterior information with insufficient internal canopy structure properties can be obtained (Balenovic et al., 2017; Kachamba et al., 2017). Therefore, the surface differencing approach that calculates the volume between the highest and lowest point of the canopy was employed to generate a CVM in this study (Eitel et al., 2014; Walter et al., 2018). Canopy volume of each biomass sampling spot was calculated by accumulating pixel-wise volume from interpolated and rasterized CHM (Fig. 2). The calculation of canopy volume is expressed as follows:

$$CVM = \sum_{i=1}^n A_i \times H_i \quad (1)$$

where CVM is the abbreviation of canopy volume model, i represents the i th pixel in CHM, n is the total number of pixels in a biomass sampling spot, A_i represents the area of pixel i , H_i represents the height of the pixel i .

Canopy volume, which indicates both vertical and horizontal properties of vegetation canopy, has been reported as a promising indicator of crop biomass (Walter et al., 2018). However, biomass samples with same canopy volumes could have different weights due to the spatial differences in leaf water content, pigment concentration, canopy architecture and species/genotypes, especially in a complex heterogeneous crop field. Spectral information can capture the differences in crop physiological state, species and genotypes, and thus provide supplementary information for the biomass estimation using canopy volume (Greaves et al., 2016). Fusion of structural metrics with spectral indices has demonstrated the ability to improve biomass estimation accuracy in previous studies (Luo et al., 2017; Maimaitjiang et al., 2017; Tilly et al., 2015).

In this work, we introduce a density factor (bulk density) for the crop, that was extracted from canopy spectral information, and it can

Table 3
Definitions of the canopy structure-based metrics.

Canopy structure-based metrics	Definition
Mean canopy height	$CH_{mean} = \left(\frac{1}{n}\right) \times \sum_{i=1}^n H_i$
Maximum canopy height	$CH_{max} = MAXH_i$
Minimum canopy height	$CH_{min} = MINH_i$
Standard deviation of canopy height	$CH_{std} = \sqrt{\left(\frac{1}{n-1}\right)} \times \sum_{i=1}^n (H_i - CH_{mean})^2$
Coefficient of variation of canopy height	$CH_{cv} = CH_{std}/CH_{mean}$
Basal area (canopy projected area)	$BA = n \times PS^2$

n is the total number of pixels in a biomass sampling spot; H_i is the height of the pixel i ; PS represents the pixel size.

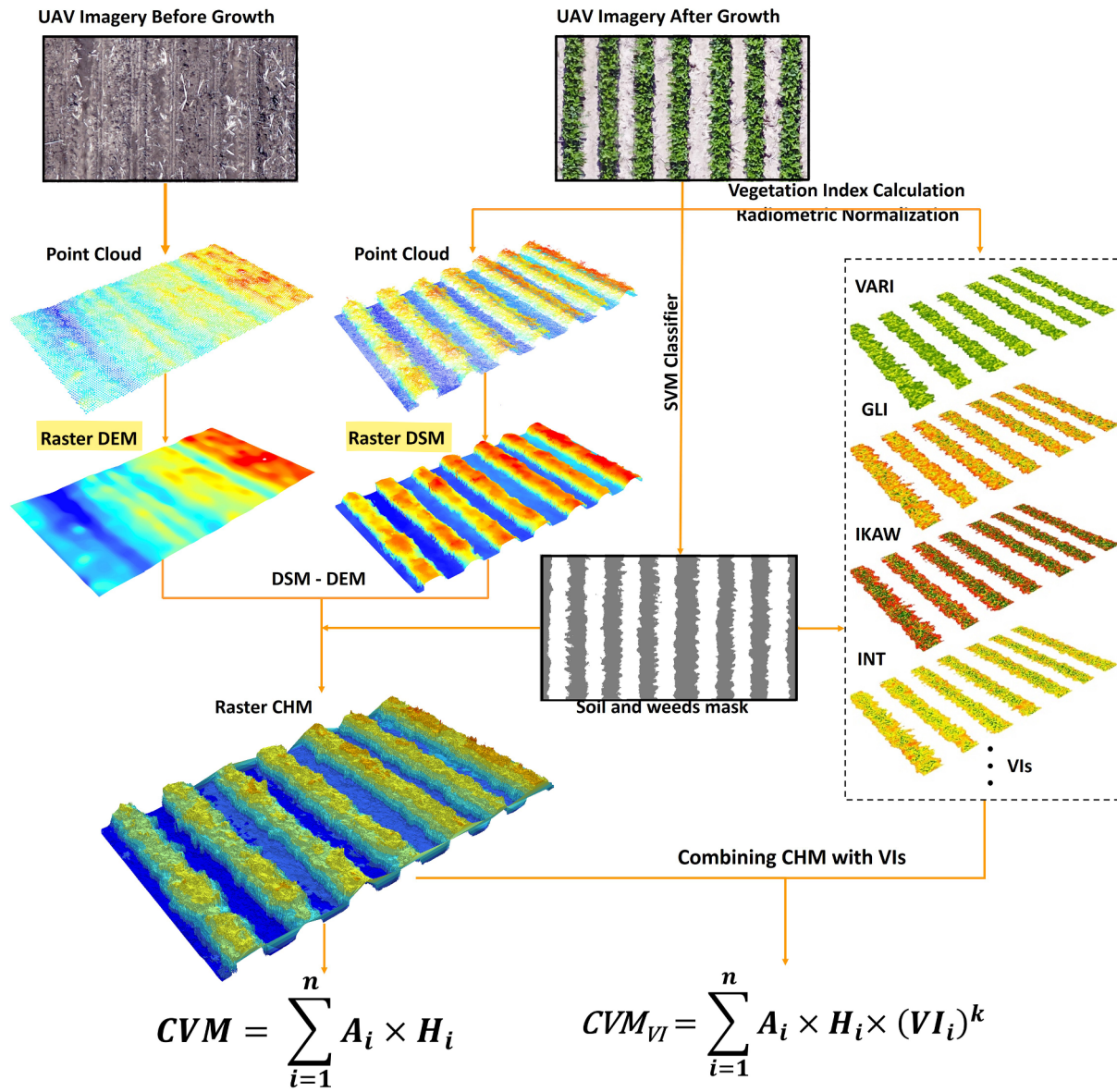


Fig. 2. The workflow diagram of the proposed CVM_{VI} for biomass estimation.

reflect vegetation physiological state and species/genotypes to some extent. The density factor is multiplied by corresponding canopy volume as a crop canopy weight to form vegetation index weighted canopy volume model (CVM_{VI}) that was used as an indicator for biomass estimation (Fig. 2), and CVM_{VI} is computed as

$$CVM_{VI} = \sum_{i=1}^n A_i \times H_i \times (VI_i)^k \quad (2)$$

where VI_i represents the vegetation index value of pixel i . $(VI_i)^k$ is the density factor and k is a constant which controls non-linearity of Eq. (2). In our experiment, it was found that $k = 1$ provides best results for AGB estimation and thus we used $k = 1$ throughout our experiments, although it can be varied based on the input data.

Crop canopy volume is a combination of plant tissue and void space. Bulk density often relates to plant architecture, tissue characteristics and leaf internal contents (Pottier and Jabot, 2017). However, bulk density used in this case may not cover all these factors. Unlike the previous studies, which combined structural metrics with spectral indices as separate input features for biomass estimation or so-called feature level data fusion (Li et al., 2016; Schaefer and Lamb, 2016; Tilly et al., 2015), CVM_{VI} is a single index level feature that incorporates

structural and spectral information.

3.3. Modelling method

Before assessing the predictability of the UAS imagery-based spectral indices, structural metrics and CVM_{VI} , the correlation between these variables and AGB was investigated through Pearson correlation and Spearman's rank-order correlation analysis with IBM SPSS software (version 24, IBM Corp., Armonk, NY, US). Pearson correlation and Spearman's rank-order correlation analysis can separately reveal the linear and monotonic relationship between the variables and AGB (Hauke and Kossowski, 2011).

Several popular regression models such as Linear, Power, Exponential, Polynomial and Logarithmic regression were implemented using UAS imagery-derived metrics CH_{mean} , BA, CVM and CVM_{VI} as input data for AGB estimation. In addition, commonly used complex regression models such as stepwise multilinear regression (SMR) and partial least squares regression (PLSR) for biomass estimation were also employed and compared using multiple spectral indices and structural metrics as input features (Deng et al., 2014; Shao and Zhang, 2016; Wang et al., 2017).

A leave-one-out cross-validation (LOOCV) method was applied for model training and validation. LOOCV excludes one sample for validation and uses the rest of the samples for training in every trial. This method can minimize overfitting and allow a more accurate assessment of model prediction strength (Wang et al., 2017; Zhu et al., 2017). To evaluate the model accuracy and robustness, the commonly used evaluation metrics, such as the coefficient of determination (R^2), root mean square error (RMSE) and relative RMSE (RRMSE) were employed. Furthermore, the average systematic error (ASE) and mean percent standard error (MPSE), which have proven to be effective metrics for plant biomass model evaluation (Zeng, 2015a,b; Zeng et al., 2016; Zeng and Tang, 2011), were computed. The evaluation metrics are expressed as follows:

$$\text{RMSE} = \sqrt{\frac{\sum_{i=1}^n (y_i - \hat{y}_i)^2}{n - 1}} \quad (3)$$

$$\text{RRMSE} = \frac{\text{RMSE}}{\bar{y}} \times 100 \quad (4)$$

$$\text{ASE} = \frac{\sum_{i=1}^n \frac{|y_i - \hat{y}_i|}{\hat{y}_i}}{n} \times 100 \quad (5)$$

$$\text{MPSE} = \frac{\sum_{i=1}^n \left| \frac{(y_i - \hat{y}_i)}{\bar{y}} \right|}{n} \times 100 \quad (6)$$

where y_i and \hat{y}_i are the measured and the predicted AGB, respectively. \bar{y} is the mean of measured AGB, and n is the total number of samples in the testing set.

The designated regression models were implemented in MATLAB R2017a on Microsoft Windows and run on a 3.4-GHz desktop computer with an Intel Xeon CPU and 80-GB RAM. All competing methods are from the associated MATLAB packages.

To investigate the performance and applicability of the proposed CVM_{VI} to different soybean genotypes, a one-way analysis of variance (ANOVA) followed by an honest significant difference (HSD) Tukey test ($\alpha = 0.05$) was conducted to test the significant differences of the estimated AGB between the three genotypes ('Pana', 'Dwight', and 'AG3432'). ANOVA test was performed using IBM SPSS software (version 24, IBM Corp., Armonk, NY, US).

4. Results

4.1. Canopy height extraction and validation

Canopy height is an important factor for estimating crop biomass (Bendig et al., 2014; Bendig et al., 2015). UAS-based photogrammetric point clouds derived CH was compared against manual, ground-based CH measurements. We found noticeable linear correlations ($R^2 = 0.898$) between ground and UAS-derived CH (Fig. 3). It should be considered that UAS-derived CH was obtained by computing the difference between DSM and DEM from SfM generated point clouds as mentioned in Section 3.1.2 with expected statistical biases (Iqbal et al., 2017). In our experiments, there were 432 CH samples, 144 for each field campaign date (08 July, 20 July and 04 August) marked as green, blue and red color dots in Fig. 3, respectively. In general, the estimated CH for all 432 samples across dates exhibits strong agreement with ground-based measurements based on the error metrics ($\text{RMSE} = 0.074 \text{ m}$). In detail, the metric ASE, which is able to reflect a summary of statistical divergence between variables to some extent, indicates that there were slightly underestimated biases in UAS-derived CH. Similar results were also observed in other studies (Bendig et al., 2014; Iqbal et al., 2017). Moreover, CH from the late developmental stage (i.e., 04 August) showed wider spread and a more stable trend compared to the other two dates, while the relatively early developmental stage (i.e., 08 July) showed more underestimation biases and

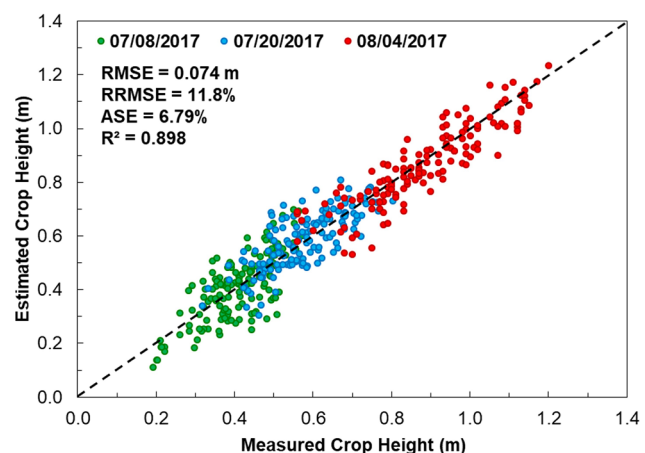


Fig. 3. Relationship between UAS-derived and field measured CH.

thus a lower correlation. This scenario is likely explained by changes in canopy structure at different developmental stages which may influence the precision of SfM generated 3D point clouds (Malambo et al., 2018).

4.2. Correlation analysis between spectral indices, structural and volumetric metrics and AGB

Correlation analysis was performed to examine the relationship between three sets of information including spectral, structural and volumetric (SSV) (Table 4). The goodness of correlation was evaluated based on the Pearson correlation and Spearman's rank-order correlation (e.g., r). In each type of correlation, three separated dates (July 8, July 20, and August 20 of 2017) of UAS data along with their combinations were used to investigate the correlation between AGB and the specified indices and metrics. In general, the combined data produced better correlation than the data captured from a single date, which could be due to the joint data containing a wider range of values that likely increased the strength of the relationship.

Comparing spectral indices with structural metrics, the latter appeared to have a stronger positive correlation to AGB than the former. In particular, the CH parameters such as the CH_{mean} produced the highest correlation ($r = 0.889$) among all spectral indices and structural metrics when using the combined data, a similar case occurred in the data from 08 July and 20 July. This indicates a strong relationship between the point clouds-derived CH and AGB (Bendig et al., 2014; Walter et al., 2018), while also demonstrating the limitation of dimensionless measures produced by VIs for interpreting canopy structure (Eitel et al., 2014); as it relates to AGB.

While CH showed a promising correlation to AGB, the volumetric metric CVM provided even higher correlation with AGB ($r = 0.924$), aligning with the work of Walter et al. (2018). One likely factor that contributes to this result is that CVM contains both CH (vertical-wise) and basal area (horizontal-wise) information which boosted the relationship. Therefore, it is reasonable to suppose that CVM can be a more suitable estimator for AGB than CH.

The correlation results of CVM_{VI} were larger than the spectral indices, structural and volumetric metrics in most of the cases. The Visible Atmospherically Resistance Index (VARI) weighted CVM (CVM_{VARI}) was found to be the best estimator ($r = 0.907$) when using data from the relatively early developmental stage (i.e., 08 July). The Vegetative Index (VEG) weighted CVM (CVM_{VEG}) provided the best correlation ($r = 0.802$) with AGB using the data captured in the medium developmental stage (i.e., 20 July), and finally the Excess Green Minus Excess Red Index (EXGR) weighted CVM (CVM_{EXGR}) correlated higher ($r = 0.691$) than other indices and metrics for the data from the later developmental stage (i.e., 04 August). Using the combined data from all three dates, the Green Red Ratio Index (GRRI) weighted CVM

Table 4Correlation coefficient (r) between image-derived information and AGB.

Spectral indices	Pearson correlation coefficient (r)				Spearman's rank-order correlation coefficient (r)			
	07/08/2017	07/20/2017	08/04/2017	All	07/08/2017	07/20/2017	08/04/2017	All
Spectral indices								
R	NS	-0.660**	-0.513*	-0.791**	NS	-0.565*	-0.413**	-0.692*
G	NS	-0.653**	-0.446**	-0.805**	NS	-0.542**	-0.331*	-0.650**
B	-0.304*	-0.514**	-0.403**	-0.540	-0.339*	-0.489*	-0.270	-0.499**
rn	-0.745**	-0.360*	-0.466*	NS	-0.769**	-0.319	-0.470**	NS
gn	0.490**	0.544**	0.325*	0.688**	0.501**	0.545**	0.332*	0.669**
bn	0.417**	NS	NS	0.754**	0.331*	NS	NS	0.776**
GRRI	0.690**	0.493**	0.535**	0.544**	0.737**	0.439**	0.578**	0.525**
GBRI	NS	0.314*	0.036	0.757**	0.180	0.376**	0.020	0.774**
RBRI	-0.448**	NS	NS	-0.687**	-0.417**	NS	NS	-0.765**
INT	NS	-0.648**	-0.477**	-0.759**	NS	-0.575**	-0.379**	-0.626**
GRVI	0.695*	0.511**	0.547**	0.437**	0.737**	0.441**	0.576**	0.427**
NDI	-0.695**	-0.511**	-0.547**	-0.438**	-0.737**	-0.439**	-0.582**	-0.428**
WI	0.665**	NS	0.309*	0.323**	0.777**	NS	0.328*	0.345**
IKAW	-0.615**	NS	NS	-0.690**	-0.582**	NS	NS	-0.745**
GLI	0.471**	0.539**	0.320*	0.700*	0.482**	0.544**	0.329*	0.677**
VARI	0.725**	0.413**	0.550**	0.291**	0.749**	0.366*	0.562**	0.266**
ExR	-0.690**	-0.524**	-0.544**	-0.432**	-0.739**	-0.445*	-0.589**	-0.419**
ExG	0.490**	0.544**	0.325*	0.688**	0.501**	0.545**	0.332*	0.669**
ExB	NS	-0.352*	NS	-0.757**	NS	-0.392**	NS	-0.765**
ExGR	0.593**	0.570**	0.450**	0.623**	0.632**	0.513**	0.427**	0.608**
VEG	0.556**	0.518**	0.404**	0.629**	0.589**	0.495**	0.406**	0.643**
IPCA	NS	-0.402**	-0.298*	-0.882**	NS	-0.287*	-0.285*	-0.815**
CIVE	NS	0.422**	NS	0.851**	NS	0.315*	NS	0.713**
COM	NS	0.439**	NS	0.851**	NS	0.334*	NS	0.714**
Structural metrics								
CH _{mean}	0.781**	0.736**	0.436**	0.889**	0.737**	0.665**	0.379**	0.911**
CH _{max}	0.635**	0.690**	0.352*	0.866**	0.716**	0.615**	0.321*	0.875**
CH _{min}	0.356*	0.752**	0.421**	0.831**	0.250	0.565**	0.368*	0.841**
CH _{std}	NS	NS	NS	NS	-0.100	-0.545**	-0.206	-0.045
CH _{cv}	-0.589**	-0.659**	-0.359*	-0.631**	-0.649**	-0.717**	-0.339*	-0.750**
BA	0.814**	0.560**	0.444**	0.814**	0.857**	0.603*	0.340*	0.891**
Proposed CVM_{VI}								
CVM	0.860**	0.774**	0.597**	0.924**	0.829**	0.718**	0.489**	0.939**
CVM _R	0.782**	0.546**	0.363*	0.581**	0.770**	0.578*	0.336*	0.653**
CVM _G	0.806**	0.582**	0.409**	0.504**	0.791**	0.600**	0.382**	0.592**
CVM _B	0.826**	0.513**	0.415**	0.641**	0.792**	0.542**	0.374**	0.716**
CVM _{rn}	0.819**	0.719**	0.511**	0.920**	0.790**	0.703**	0.418**	0.937**
CVM _{gn}	0.850**	0.773**	0.629**	0.903**	0.828**	0.730**	0.530**	0.922**
CVM _{bn}	0.862*	0.694*	0.514**	0.921**	0.840**	0.681*	0.441**	0.943**
CVM _{GRRI}	0.817**	0.705**	0.686**	0.947**	0.794**	0.692**	0.585**	0.949**
CVM _{BGRI}	0.859**	0.657**	0.499**	0.921**	0.838**	0.662**	0.438**	0.942**
CVM _{RBRI}	0.685**	0.494**	0.515**	0.758**	0.704**	0.512**	0.468**	0.802**
CVM _{INT}	0.805**	0.561**	0.399**	0.569**	0.791**	0.575**	0.358*	0.644**
CVM _{GRVI}	0.873**	0.753**	0.611**	0.692**	0.865**	0.695**	0.587**	0.754**
CVM _{NDI}	-0.872**	-0.753**	-0.611**	-0.691**	-0.865**	-0.695**	-0.587**	-0.753**
CVM _{WI}	-0.699**	-0.525*	-0.343*	-0.888**	-0.673**	-0.542**	-0.308*	-0.914**
CVM _{IKAW}	0.669**	0.424**	NS	0.574**	0.701**	0.441**	NS	0.656**
CVM _{GLI}	0.849**	0.784**	0.584**	0.751**	0.836**	0.743**	0.523**	0.811**
CVM _{VARI}	0.907**	0.685**	0.599**	0.756**	0.875**	0.625**	0.553**	0.804**
CVM _{ExR}	-0.818**	-0.584**	NS	0.591**	-0.816**	-0.462*	NS	0.527**
CVM _{ExG}	0.849**	0.786**	0.589**	0.710**	0.841**	0.738**	0.534**	0.774**
CVM _{ExB}	-0.798**	-0.701**	-0.282	-0.175*	-0.812**	-0.704**	-0.300*	-0.294**
CVM _{ExGR}	0.856*	0.779*	0.691**	0.507**	0.856**	0.735*	0.654**	0.599**
CVM _{VEG}	0.880**	0.802**	0.637**	0.855**	0.845**	0.761**	0.587**	0.893**
CVM _{IPCA}	0.770**	0.590**	0.328*	0.221**	0.772**	0.617**	0.358*	0.358**
CVM _{CIVE}	-0.773**	-0.460**	-0.301*	-0.509**	-0.778**	-0.475*	NS	-0.419**
CVM _{COM}	-0.765**	-0.426**	-0.354*	-0.540**	-0.780**	-0.430*	-0.305*	-0.425**

The highest r value for each type of metrics is highlighted in boldface.

Description for each index and metric referred to Table 2.

** Correlation is significant at the 0.01 level (2-tailed).

* Correlation is significant at the 0.05 level (2-tailed); NS represents not significant.

(CVM_{GRRI}) turned out to be the best indicator ($r = 0.947$) for AGB estimation.Multi-temporal screening of correlation analysis showed that both Pearson and Spearman's rank-order correlation analysis based coefficient values decreased from July 8 to August 4 for spectral indices and structural metrics, as well as CVM and proposed CVM_{VI} in most of thecases (Table 4). This may be due to the saturation issue of spectral indices in response to the change of biomass to higher vegetation density (Zhao et al., 2016). Additionally, lack of canopy structural information at vertical sides because of sensor-view occlusion due to high density and canopy closure at late developmental stages may also result in lower accuracy of CVM and CVM_{VI}.

Table 5

Validation statistics of univariate and multivariate regression models for AGB estimation (The best model for using each type of input variables is highlighted in boldface).

Input variables	Model		R ²	RMSE (kg/m ²)	RRMSE (%)	ASE (%)	MPSE (%)
CH _{mean}	Linear	$y = 0.0491 \times x - 0.903$	0.785	0.263	22.0	13.83	41.6
	Power	$y = 0.0403 \times x^{1.04} - 0.804$	0.783	0.264	22.0	9.85	39.0
	Exponential	$y = 0.552 \times \exp(0.0204 \times x)$	0.710	0.309	25.8	-7.93	28.1
	Polynomial	$y = -1.21e-05 \times x^3 + 2.15e-03 \times x^2 - 7.94e-02 \times x + 1.23$	0.801	0.258	21.6	0.71	25.8
	Logarithmic	$y = \exp(1.67 \times \ln(x) - 6.24)$	0.769	0.265	22.1	5.21	26.1
BA	Linear	$y = 2.38 \times x - 1.20$	0.650	0.358	29.9	-8.84	34.5
	Power	$y = 0.726 \times x^{2.492} + 0.234$	0.688	0.311	26.0	0.84	26.4
	Exponential	$y = -6.03e-16 \times \exp(18.1 \times x) + 0.168 \times \exp(1.71 \times x)$	0.702	0.300	25.1	4.33	27.6
	Polynomial	$y = 1.47 \times x^2 - 1.07 \times x + 0.546$	0.691	0.311	26.0	0.75	26.7
	Logarithmic	$y = \exp(1.62 \times \ln(x) + 0.0812)$	0.682	0.338	28.2	7.18	31.5
CVM	Linear	$y = 2.31 \times x - 0.00823$	0.848	0.227	19.0	4.96	23.9
	Power	$y = 0.726 \times x^{1.13} + 0.165$	0.849	0.225	18.7	0.49	20.8
	Exponential	$y = 0.738 \times \exp(1.01 \times x)$	0.799	0.257	21.4	-7.29	24.3
	Polynomial	$y = 0.159 \times x^2 + 2.02 \times x + 0.0864$	0.847	0.225	18.8	1.25	20.9
	Logarithmic	$y = \exp(0.901 \times \ln(x) + 0.787)$	0.847	0.225	18.8	3.78	21.7
CVM _{GRRI}	Linear	$y = 2.10 \times x + 0.0912$	0.893	0.194	16.3	1.43	19.5
	Power	$y = 2.81 \times x^{1.09} + 0.206$	0.892	0.196	16.4	0.02	19.3
	Exponential	$y = 0.763 \times \exp(1.29 \times x)$	0.852	0.234	19.6	-6.56	22.9
	Polynomial	$y = 0.201 \times x^2 + 2.65 \times x + 0.159$	0.892	0.196	16.4	0.21	19.3
	Logarithmic	$y = \exp(0.873 \times \ln(x) + 1.06)$	0.890	0.200	16.7	3.23	20.1
CH _{mean} + BA + GRRI	SMR	/	0.890	0.199	16.7	1.64	20.0
	PLSR (PCs = 3)	/	0.872	0.223	18.7	11.51	36.7
All Spec. + Struc.	SMR	/	0.915	0.169	14.1	1.51	17.9
	PLSR (PCs = 7)	/	0.911	0.177	14.8	8.55	26.4

PCs: principal components. Spec. and Struc. represent all spectral indices and structural metrics, respectively in Table 4.

4.3. Biomass modelling

A leave-one-out cross-validation (LOOCV) method was applied for model training and validation due to its capability in unbiased assessment of a model (Cawley and Talbot, 2003). The results for AGB estimation were evaluated by R², RMSE, RRMSE, ASE, and MPSE (Table 5). We tested several popular regression models, such as linear regression (LR), power regression, exponential regression, polynomial regression (PR), logarithmic regression, SMR and PLSR to investigate the importance of related indices and metrics for AGB prediction. Note that the number of principal components (PCs) in PLSR was tuned, and the optimal number of PCs was found to be 3 and 7 for the cases of 3 (CH_{mean}, BA and GRRI) input variables and 30 (spectral indices and structural metrics in Table 4) input variables, respectively.

The developed model equations and their corresponding validation metrics are presented in Table 5. It is worth noting that the LOOCV approach, which excludes one sample for validation and uses the rest of the samples for training in every trial, generates a model in each trial. In other words, since there are 144 AGB samples in our dataset, there will be 144 models when using LOOCV approach, which results in 144 evaluation metrics, such as R², RMSE, RRMSE, ASE, and MPSE, for a regression method. In Table 5, we randomly selected one model for each regression method to demonstrate its expression, and the average value of R², RMSE, RRMSE, ASE, and MPSE over 144 trials was calculated, respectively. The best estimate of AGB from different input variables was compared with corresponding measured values using 1:1 scatterplot (Fig. 4). Clearly, the linear regression with the proposed CVM_{VI}, which combined canopy SSV information, yielded the highest R² value (0.893) as well as the lowest prediction errors (RRMSE = 16.3%, MPSE = 19.5%) when only one variable was used as a predictor. CVM which contains both the canopy horizontal and vertical structural information performed superior to CH_{mean} and BA metrics with R² value of 0.849, RRMSE value of 18.7% and MPSE value of 20.8%, respectively. These results emphasize the value of the SSV combination based CVM_{VI} for AGB (Fig. 4). In contrast, the 2D structural metrics CH_{mean} and BA, which tend to have a nonlinear

correlation with AGB, resulted in lower accuracy when using LR for AGB estimation and slightly higher accuracy using nonlinear regression such as PR.

To further assess the capability of CVM_{VI}, two complex multivariate models SMR and PLSR were employed and tested as follows: (1) the three variables CH_{mean}, BA and GRRI which formed CVM_{VI} were used as separate input to SMR and PLSR; and (2) all spectral indices and structural metrics listed in Table 4 served as input. In the first case, CVM_{GRRI} with linear regression (CVM_{GRRI}-LR) outperformed both SMR and PLSR, even though three variables were used to predict AGB while CVM_{GRRI}-LR used only one input. In the second case, the accuracy of CVM_{GRRI}-LR was slightly lower than SMR using all spectral indices and structural metrics. However, there was only one variable used as the predictor in CVM_{GRRI}-LR which is computationally simple and efficient compared to multivariate complex regression models. These results emphasize the potential of CVM_{VI} as a single and simple indicator for biomass estimation in the context of high-throughput phenotyping.

In summary, CVM and the proposed CVM_{VI} proved to be more effective than other spectral indices or structural metrics for soybean AGB prediction.

5. Discussion

5.1. Performance comparison of simple models and complex models for AGB estimation

The superior performance of CVM compared to CH and BA in AGB estimation may be explained by the complex 3D canopy characteristics of AGB (Walter et al., 2018). Additionally, when implemented at high spatial resolution, CVM involves canopy structure traits in both vertical and horizontal dimensions (Greaves et al., 2016). In accordance with previous studies (Bendig et al., 2014; Bendig et al., 2015), the potential of CH and BA in biomass estimation was demonstrated. However, CH and BA only include one-dimensional information about the plant canopy which tend to saturate as biomass increases. For example, as seen in Fig. 4, CH and BA based models underestimated most of the samples

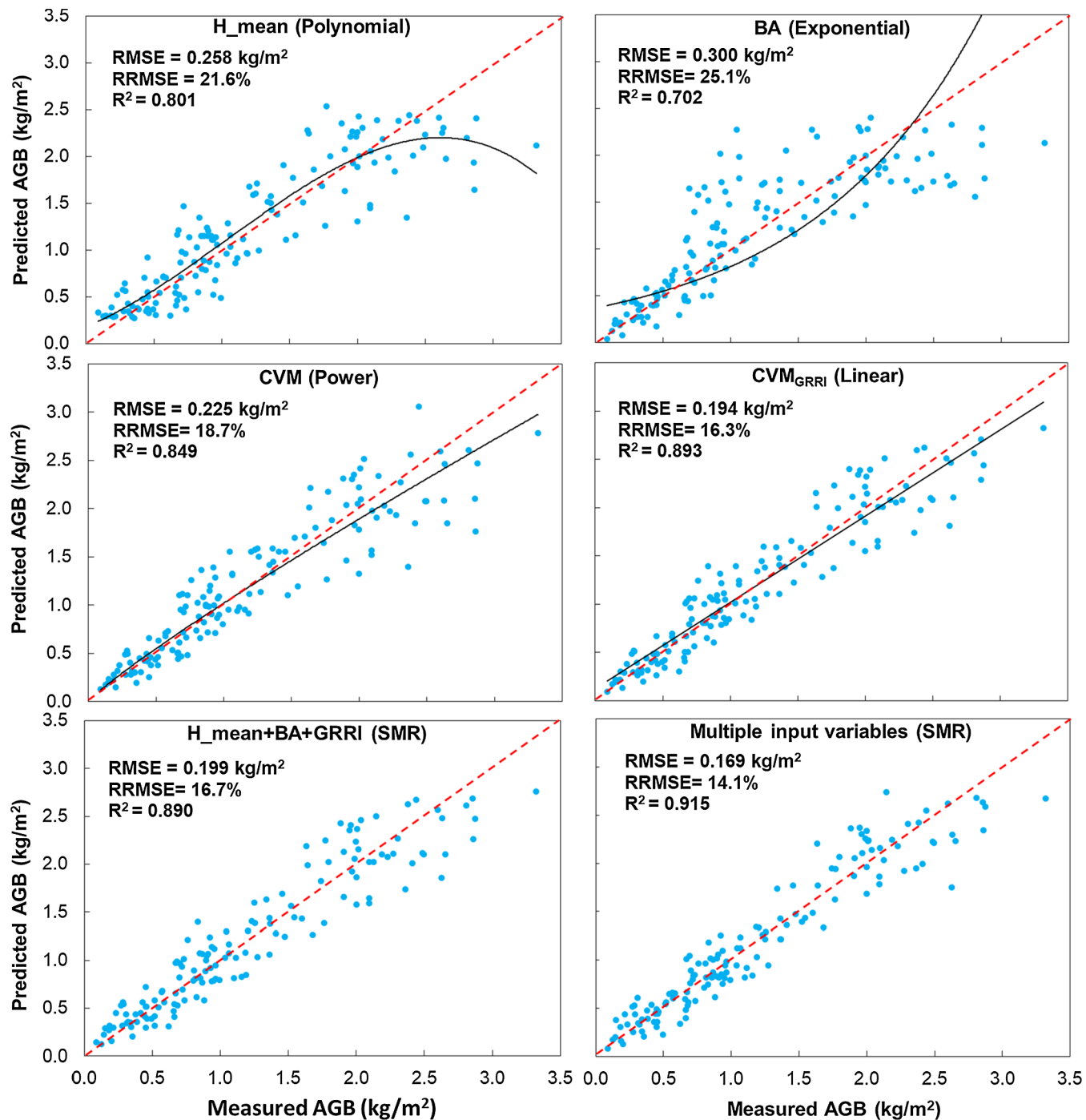


Fig. 4. The cross-validation scatter-plots for field-measured versus predicted AGB.

with AGB higher than 2.5 kg/m². It is worth noting that SfM based point clouds are generated from the canopy surface and volumetric based biomass estimation methods assume that biomass-per-volume is constant (Greaves et al., 2015; Li et al., 2016).

Incorporating VIs into CVM further improved the estimation of soybean AGB, decreasing RMSE by about 0.030 kg/m² (5% of RRMSE) and increasing R² by about 0.050 (Table 5), which generally aligns with results found in other crop biomass estimation studies. Studies focusing on the application of LiDAR in crop biomass estimation are limited, likely due to the requirement for dense point clouds and the previously mentioned high sensor costs and operational complexity. Wang et al. (2017) reported that incorporating spectral information into LiDAR-derived estimates of maize biomass improved the model R² from 0.835

to 0.883. Similarly, Li et al. (2016) found the spectral index GRVI as the second-best predictor (CH_{mean} was the best predictor) in the estimation of maize (*Zea mays* L.) AGB. Generally, our study is another case that revealed the complementary relationships between spectral and structural information using one simple model (CVM_{VI}). However, VIs are impacted by varying irradiance that introduces bidirectional reflectance distribution function (BRDF) and multangular reflection effects (Damm et al., 2015; Li et al., 2016; Tilly et al., 2015). Therefore, modeling errors caused by these effects warrant further thorough investigations. CVM_{VI}-LR also outperformed statistically more complex regression models such as SMR and PLSR which used CH_{mean}, BA and GRRI as input variables. This finding is attributable to the spatial heterogeneity of canopy structure that was captured in CVM.

Table 6

Validation statistics for AGB estimation using CVM_{VI}-LR for different genotypes and developmental stages.

Data	Independent variable	R ²	RMSE (kg/m ²)	RRMSE (%)	ASE (%)	MPSE (%)
Dwight	CVM _{GRRI}	0.913	0.182	17.0	16.9	35.9
Pana	CVM _{GRRI}	0.904	0.165	15.3	0.877	18.2
AG3432	CVM _{GRRI}	0.889	0.200	13.8	1.58	15.7
07/08/2017	CVM _{VARI}	0.804	0.088	18.9	0.543	22.6
07/20/2017	CVM _{VEG}	0.614	0.137	13.8	0.571	13.7
08/04/2017	CVM _{ExGR}	0.432	0.274	12.8	0.215	13.0
All data	CVM _{GRRI}	0.893	0.194	16.3	1.43	19.5

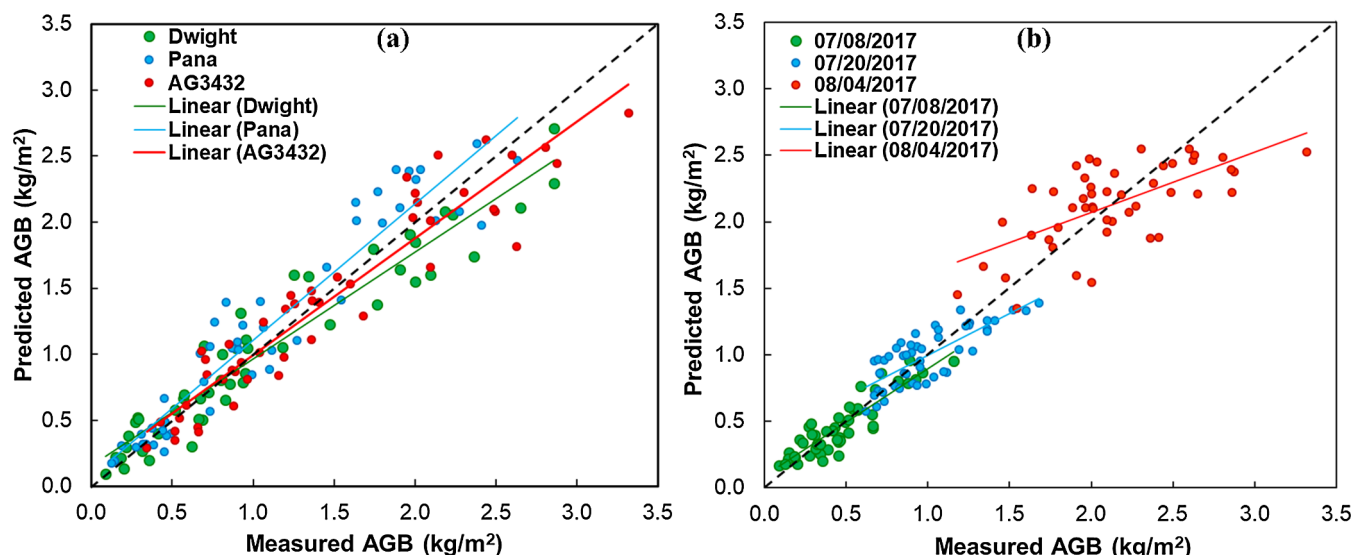


Fig. 5. Measured vs. predicted AGB from LR model for different genotypes (a), and developmental stages (b).

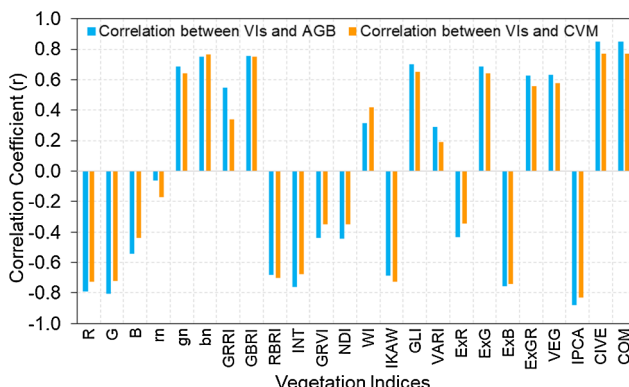


Fig. 6. Correlation relationship of VIs to AGB and CVM.

5.2. CVM_{VI} performance for AGB estimation for different genotypes and developmental stages

The robustness of the proposed approach for AGB estimation was evaluated by implementing the CVM_{VI} for estimating the AGB by soybean genotype and developmental stage, respectively (Table 6). The CVM_{VI} performed equally well in estimating the AGB of different soybean genotypes (R^2 ranged from 0.913 to 0.889, Table 6 and Fig. 5a). However, this was not the case at the different developmental stages as shown by the decrease in R^2 from 0.804 on July 8 to 0.432 on August 4 (Table 6 and Fig. 5b). Compared to ALS or TLS, photogrammetric point clouds provide exterior canopy surface information due to insufficient penetration capability and the increasing of canopy density and closure from July 8 to August 4. Thus, structural characteristics from canopy

sides cannot be detected by digital cameras, which may lead to less accuracy of CVM, especially at relatively late developmental stages. In addition, the well-recognized saturation issue of optical sensors can cause lower sensitivity of VIs to the change in biomass of dense vegetation. This may be another key factor causing inaccurate AGB estimates using CVM_{VI} at relatively late developmental stages (Zhao et al., 2016).

The performance and applicability of CVM_{VI} to detect AGB differences across the genotypes was evaluated using ANOVA with HSD Tukey tests ($\alpha = 0.05$). ANOVA test shows that the predicted AGB for genotypes 'Dwight' and 'AG3432' is significantly different ($p < 0.05$), while no significant differences were found between the predicted AGB of 'Dwight' and 'Pana', and 'Pana' and 'AG3432', respectively. This is consistent with the measured AGB for the three genotypes, which indicates that the proposed CVM_{VI} shows the effectiveness to distinguish AGB differences between the genotypes to some extent, future research should test the CVM_{VI} method with a large number of soybean genotypes to explore the suitability for high-throughput AGB phenotyping.

5.3. Performance of different vegetation indices for weighting CVM to build CVM_{VI}

A variety of VIs were extracted for CVM_{VI} computation. The GRRI weighted CVM (CVM_{GRRI}) yielded the best linear and non-linear correlation coefficient with AGB (Table 4), and proved to be the optimal single metric for AGB estimation (Table 5 & Fig. 4). Canopy volume often has a positive correlation with vegetation AGB (Walter et al., 2018), and the appropriate VIs which was regarded as bulk density factor also needed to be positively correlated with AGB (Fig. 6). Otherwise, CVM and VIs may offset each other in biomass estimation to some extent. This can be noticed in Table 4 where CVM_{VIs} using VIs that

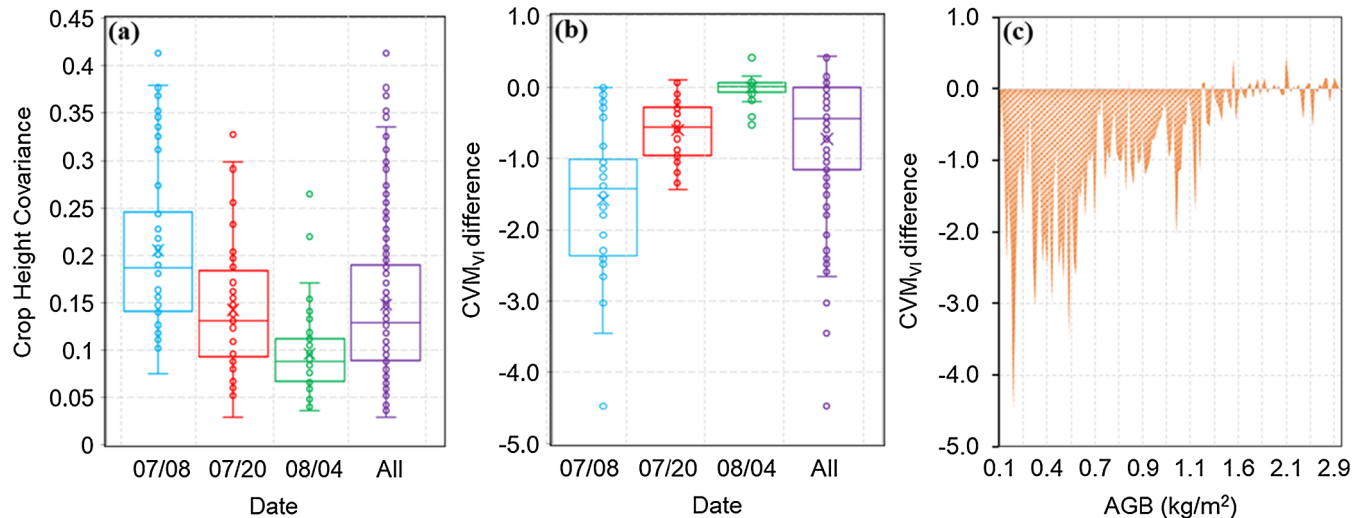


Fig. 7. Canopy height covariance (a); the accumulation and averaging approach-based CVM_{VI} difference on different sampling days/developmental stages (b), and at different level of AGB weights (c).

Table 7

Validation results for AGB estimation using different CVM_{VI} calculating approaches (LR model).

CVM _{VI} calculation methods	R ²	RMSE (kg/m ²)	RRMSE (%)	ASE (%)	MPSE (%)
Accumulation approach based CVM _{VI}	0.893	0.194	16.3	1.43	19.5
Averaging approach based CVM _{VI}	0.880	0.204	17.2	1.58	20.0

are negatively correlated with AGB result in lower correlations with AGB. In addition, to avoid or reduce the collinearity issues in AGB estimation using CVM_{VI}, the optimal VI for weighting CVM needs to be identified. Correlation coefficients between VIs and AGB and CVM are shown in Fig. 6 and illustrate that some VIs such as CIVE, COM etc., were highly positively correlated with AGB, and CVM. Such strong correlations may contribute to the lower correlations between CVM_{CIVE}, CVM_{COM} etc., and AGB that are shown in Table 4. On the other hand, VIs such as GRRI, that are strongly correlated with AGB and less so with CVM, produced high correlations with AGB (i.e. of CVM_{GRRI} vs AGB). Moreover, it is noteworthy that GRRI weighted CVM (CVM_{GRRI}) outperformed all other CVM_{VI} when using samples from multi-temporal data (Tables 4 & 6). This likely was because ratio based VIs such as GRRI may be comparatively less sensitive to changes in illumination and atmospheric condition over time (Galvao et al., 2013).

We examined only RGB imagery-based VIs to estimate the crop canopy bulk density factor. VIs utilizing near-infrared and shortwave-infrared regions of the spectrum should be investigated in future work, and canopy thermal information and LiDAR intensity information can also be examined as bulk density factor. Additionally, metrics used as bulk density factor need to be tested for different crop species.

5.4. Advantages of CVM_{VI} from pixel-wise accumulation approach

In previous studies, CH and VIs values were averaged for each sampling spot for biomass estimation (Bendig et al., 2015; Tilly et al., 2015). The CVM_{VI} method applied in this study utilized the accumulation of CH and VIs values of all pixels within each biomass sampling spot instead of using a mean value (Eq. (2)). Compared to averaging CH and VIs values, the accumulation approach better characterizes the surface roughness of crop canopy and heterogeneity of VIs within each sampling spot. To investigate the advantages of this accumulation approach compared to the approach that uses average CH and VIs (averaging approach), the mean CH and VIs values of all pixels within each sampling spot were calculated to construct the averaging-based CVM_{VI} by

$$CVM_{VI} = BA \times CH_{mean} \times (VI_{mean})^k \quad (7)$$

where BA represents the projected canopy basal area of each sampling spot, CH_{mean} and VI_{mean} represent average CH and VI values of all pixels within each sampling spot; k is a constant which controls non-linearity, and k = 1 was employed for consistency with Eq. (2).

The differences between the accumulation and averaging approaches-based CVM_{VI} on different sampling days/developmental stages (Fig. 7b), and at different level of AGB weights (Fig. 7c), were investigated. The values of accumulation-based CVM_{VI} were lower than averaging-based CVM_{VI}, especially at relatively early developmental stages (Fig. 7b) and for smaller AGB (Fig. 7c). However, the differences between the CVM_{VI} determined based on these two approaches decreased from the first sampling (i.e., 08 July) to last sampling (i.e., 04 August) (Fig. 7b), and from lower AGB to greater AGB (Fig. 7c). This is likely explained by the change of canopy surface roughness represented by the covariance of crop height (Bryant et al., 2007), which decreased from the relatively early developmental stage to the late stage (Fig. 7a).

Estimations of AGB based on the accumulation and the averaging-based CVM_{VI} were compared (Table 7), revealing that the accumulation-based CVM_{VI} achieved better performance in AGB prediction as indicated by higher R² and lower RRMSE and MPSE. This indicates that the accumulation based CVM_{VI} can better characterize canopy 3D characteristics and spectral properties, while averaging based CVM_{VI} may overestimate those properties.

5.5. Impact of spatial resolution

A simulation analysis was conducted to examine the effect of the spatial resolution of UAS imagery on the performance of CVM_{VI} for AGB estimation. The original spatial resolution (0.006 m) of the raw RGB images was degraded to 0.020 m, 0.050 m, 0.100 m, 0.150 m, 0.200 m, and all other processing steps and CVM_{GRRI} calculation were applied accordingly. The result shows that the accuracy of the CVM_{GRRI}-LR based AGB estimation decreases with the degradation of image spatial resolution (Fig. 8). More specifically, R² drops from 0.893 (i.e.,

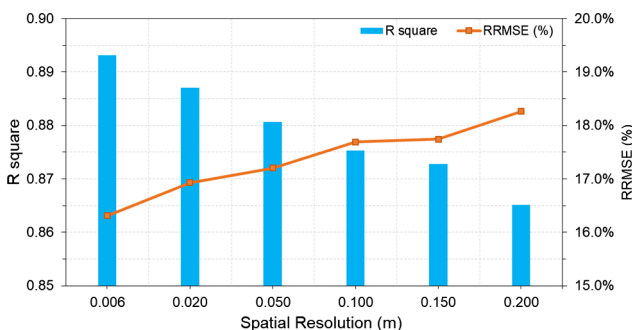


Fig. 8. The impact of different spatial resolution on the performance of CVM_{VI} for AGB estimation.

Table 8

Validation results for AGB estimation using LR model based on different resolution of CVM_{GRRI}.

Resolution	R ²	RMSE (kg/m ²)	RRMSE (%)	ASE (%)	MPSE (%)
0.006 m	0.893	0.194	16.3	1.43	19.5
0.020 m	0.887	0.202	16.9	1.14	22.4
0.050 m	0.881	0.206	17.2	0.749	22.5
0.100 m	0.875	0.212	17.7	0.878	22.7
0.150 m	0.873	0.213	17.8	1.22	22.8
0.200 m	0.865	0.218	18.3	0.590	22.9

0.006 m) to 0.865 (i.e., 0.200 m), while RRMSE increases from 16.3% (i.e., 0.006 m) to 18.3% (i.e., 0.200 m). In addition, MPSE increases continuously from 19.5% to 22.9% (Table 8). This is likely due to the fact that when the resolution of images is degraded, the photogrammetric point cloud density decreases accordingly (Fonstad et al., 2013), and thus the accuracy of CHM and CVM in characterizing canopy surface details and 3D properties of canopy structures also decreases. Moreover, with degrading the spatial resolution, the number of mixed pixels increased, which further impacted the value of CVM and VIs and led to a lower AGB estimation accuracy.

It is worth mentioning that this simulation method is not able to account for all impacts caused by different flight altitudes. For instance, a fixed camera field of view (FOV) combined with image acquisition from a higher altitude reduces the capture of information about canopy vertical sides. In such a case, the performance of CVM and CVM_{VI} can be further degraded.

6. Conclusion

This study presents an efficient approach for using low-cost, high-resolution UAS RGB imagery to accurately estimate soybean AGB. Spectral, structural and volumetric information, as well as canopy spectral and volumetric combined CVM_{VI} derived from UAS-based orthomosaics and photogrammetric point clouds are highly viable for the estimation of AGB. Compared to 2D canopy metrics such as CH and BA, photogrammetric point clouds-derived 3D CVM produced good predictions of soybean AGB. Furthermore, CVM_{VI}, which incorporates vegetation indices (particularly GRRI) with CVM, improved AGB estimation accuracy. CVM_{VI} utilized a single input variable and yielded a prediction accuracy equivalent to those of complex models (e.g., SMR and PLSR) which employ multiple spectral and structural input variables. The proposed CVM_{VI} is a simple but efficient metric for plant scientists, and may be useful for high-throughput crop biomass phenotyping and precision agriculture.

The simple and low-cost procedures that were used to track the positions of CH and biomass samplings, and the radiometric RGB image normalization employed in this study, can be replicated easily and

could benefit ground data and UAS imagery collection for relevant studies.

The results presented in this study demonstrate the great potential of the proposed CVM_{VI} as a single predictor for soybean AGB estimation. However, to further explore its utility and robustness in AGB estimation for high-throughput phenotyping, it needs to be tested for more soybean genotypes. Given the success with estimation of soybean AGB, the CVM_{VI} approach holds significant promise, and should be tested, for the estimation of AGB of other crop/plant species.

Acknowledgement

This work was supported in part by the National Science Foundation (IIA-1355406 and IIA-1430427), and in part by the National Aeronautics and Space Administration (NNX15AK03H). The authors thank Ahmad Daloye, Alissa Benchimol and Siming Lu from Saint Louis University who assisted long and strenuous hours for field data collection. The authors also thank the editor and the anonymous reviewers for their thoughtful review and constructive comments.

References

- Ahmad, I.S., Reid, J.F., 1996. Evaluation of color representations for maize images. *J. Agric. Eng. Res.* 63, 185–195.
- Araus, J.L., Cairns, J.E., 2014. Field high-throughput phenotyping: the new crop breeding frontier. *Trends Plant Sci.* 19, 52–61.
- Avitabile, V., Baccini, A., Friedl, M.A., Schmullius, C., 2012. Capabilities and limitations of Landsat and land cover data for aboveground woody biomass estimation of Uganda. *Remote Sens. Environ.* 117, 366–380.
- Avolio, M.L., Hoffman, A.M., Smith, M.D., 2018. Linking gene regulation, physiology, and plant biomass allocation in *Andropogon gerardii* in response to drought. *Plant Ecol.* 219, 1–15.
- Balenovic, I., Milas, A.S., Marjanovic, H., 2017. A comparison of stand-level volume estimates from image-based canopy height models of different spatial resolutions. *Remote Sens.* 9.
- Becker-Reshef, I., Vermote, E., Lindeman, M., Justice, C., 2010. A generalized regression-based model for forecasting winter wheat yields in Kansas and Ukraine using MODIS data. *Remote Sens. Environ.* 114, 1312–1323.
- Bendig, J., Bolten, A., Bennertz, S., Broscheit, J., Eichfuss, S., Bareth, G., 2014. Estimating biomass of barley using crop surface models (CSMs) derived from UAV-based RGB imaging. *Remote Sens.* 6, 10395–10412.
- Bendig, J., Yu, K., Aasen, H., Bolten, A., Bennertz, S., Broscheit, J., Gnyp, M.L., Bareth, G., 2015. Combining UAV-based plant height from crop surface models, visible, and near infrared vegetation indices for biomass monitoring in barley. *Int. J. Appl. Earth Obs. Geoinf.* 39, 79–87.
- Bryant, R., Moran, M.S., Thoma, D.P., Collins, C.D.H., Skirvin, S., Rahman, M., Slocum, K., Starks, P., Bosch, D., Dugo, M.P.G., 2007. Measuring surface roughness height to parameterize radar backscatter models for retrieval of surface soil moisture. *IEEE Geosci. Remote Sens. Lett.* 4, 137–141.
- Busemeyer, L., Ruckelshausen, A., Muller, K., Melchinger, A.E., Alheit, K.V., Maurer, H.P., Hahn, V., Weissmann, E.A., Reif, J.C., Wurschum, T., 2013. Precision phenotyping of biomass accumulation in triticale reveals temporal genetic patterns of regulation. *Sci. Rep.* 3.
- Cawley, G.C., Talbot, N.L., 2003. Efficient leave-one-out cross-validation of kernel fisher discriminant classifiers. *Pattern Recogn.* 36, 2585–2592.
- Clark, M.J., Roberts, D.A., Ewel, J.J., Clark, D.B., 2011. Estimation of tropical rain forest aboveground biomass with small-footprint lidar and hyperspectral sensors. *Remote Sens. Environ.* 115, 2931–2942.
- Claverie, M., Demarez, V., Duchemin, B., Hagolle, O., Ducrot, D., Marais-Sicre, C., Dejoux, J.F., Huc, M., Keravec, P., Beziat, P., Fieuza, R., Ceschia, E., Dedieu, G., 2012. Maize and sunflower biomass estimation in southwest France using high spatial and temporal resolution remote sensing data. *Remote Sens. Environ.* 124, 844–857.
- Cortes, C., Vapnik, V., 1995. Support-vector networks. *Mach. Learn.* 20, 273–297.
- Damm, A., Guanter, L., Verhoef, W., Schläpfer, D., Garbari, S., Schaepman, M., 2015. Impact of varying irradiance on vegetation indices and chlorophyll fluorescence derived from spectroscopy data. *Remote Sens. Environ.* 156, 202–215.
- Dandois, J.P., Ellis, E.C., 2013. High spatial resolution three-dimensional mapping of vegetation spectral dynamics using computer vision. *Remote Sens. Environ.* 136, 259–276.
- de Carvalho, O.A., Guimaraes, R.F., Silva, N.C., Gillespie, A.R., Gomes, R.A.T., Silva, C.R., de Carvalho, A.P.F., 2013. Radiometric normalization of temporal images combining automatic detection of pseudo-invariant features from the distance and similarity spectral measures, density scatterplot analysis, and robust regression. *Remote Sens.* 5, 2763–2794.
- Deng, S.Q., Katoh, M., Guan, Q.W., Yin, N., Li, M.Y., 2014. Estimating forest aboveground biomass by combining ALOS PALSAR and worldview-2 data: a case study at Purple Mountain National Park, Nanjing, China. *Remote Sens.* 6, 7878–7910.
- Djomo, A.N., Chimi, C.D., 2017. Tree allometric equations for estimation of above, below and total biomass in a tropical moist forest: case study with application to remote

- sensing. *For. Ecol. Manage.* 391, 184–193.
- Donald, W.W., 2006. Estimated corn yields using either weed cover or rated control after pre-emergence herbicides. *Weed Sci.* 54, 373–379.
- Du, M.M., Noguchi, N., 2017. Monitoring of wheat growth status and mapping of wheat yield's within-field spatial variations using color images acquired from UAV-camera system. *Remote Sens.* 9.
- Du, Y., Teillet, P.M., Cihlar, J., 2002. Radiometric normalization of multitemporal high-resolution satellite images with quality control for land cover change detection. *Remote Sens. Environ.* 82, 123–134.
- Eitel, J.U.H., Magney, T.S., Vierling, L.A., Brown, T.T., Huggins, D.R., 2014. LiDAR based biomass and crop nitrogen estimates for rapid, non-destructive assessment of wheat nitrogen status. *Field Crops Res.* 159, 21–32.
- Ene, L.T., Gobakken, T., Andersen, H.E., Naesset, E., Cook, B.D., Morton, D.C., Babcock, C., Nelson, R., 2018. Large-area hybrid estimation of aboveground biomass in interior Alaska using airborne laser scanning data. *Remote Sens. Environ.* 204, 741–755.
- Erdody, T.L., Moskal, L.M., 2010. Fusion of LiDAR and imagery for estimating forest canopy fuels. *Remote Sens. Environ.* 114, 725–737.
- Fonstad, M.A., Dietrich, J.T., Courville, B.C., Jensen, J.L., Carboneau, P.E., 2013. Topographic structure from motion: a new development in photogrammetric measurement. *Earth Surf. Proc. Land.* 38, 421–430.
- Galvao, L.S., Breunig, F.M., dos Santos, J.R., de Moura, Y.M., 2013. View-illumination effects on hyperspectral vegetation indices in the Amazonian tropical forest. *Int. J. Appl. Earth Obs. Geoinf.* 21, 291–300.
- Getelson, A.A., Kaufman, Y.J., Stark, R., Rundquist, D., 2002. Novel algorithms for remote estimation of vegetation fraction. *Remote Sens. Environ.* 80, 76–87.
- Gonzalez de Tanago, J., Lau, A., Bartholomew, H., Herold, M., Avitabile, V., Raumonen, P., Martius, C., Goodman, R.C., Disney, M., Manuri, S., 2017. Estimation of above-ground biomass of large tropical trees with terrestrial LiDAR. *Methods Ecol. Evolut.*
- Greaves, H.E., Vierling, L.A., Eitel, J.U.H., Boelman, N.T., Magney, T.S., Prager, C.M., Griffin, K.L., 2015. Estimating aboveground biomass and leaf area of low-stature Arctic shrubs with terrestrial LiDAR. *Remote Sens. Environ.* 164, 26–35.
- Greaves, H.E., Vierling, L.A., Eitel, J.U.H., Boelman, N.T., Magney, T.S., Prager, C.M., Griffin, K.L., 2016. High-resolution mapping of aboveground shrub biomass in Arctic tundra using airborne lidar and imagery. *Remote Sens. Environ.* 184, 361–373.
- Guarro, M., Pajares, G., Riñoros, I., Herrera, P.J., Burgos-Artizú, X.P., Ribeiro, A., 2011. Automatic segmentation of relevant textures in agricultural images. *Comput. Electron. Agric.* 75, 75–83.
- Hague, T., Tillett, N., Wheeler, H., 2006. Automated crop and weed monitoring in widely spaced cereals. *Precis. Agric.* 7, 21–32.
- Hauke, J., Kossowski, T., 2011. Comparison of values of Pearson's and Spearman's correlation coefficients on the same sets of data. *Quaestiones Geographicae* 30, 87–93.
- Hensgen, F., Buhle, L., Wachendorf, M., 2016. The effect of harvest, mulching and low-dose fertilization of liquid digestate on above ground biomass yield and diversity of lower mountain semi-natural grasslands. *Agric. Ecosyst. Environ.* 216, 283–292.
- Huang, S.C., Wang, H.W., 2006. Combining time-scale feature extractions with SVMs for stock index forecasting. *Neural Information Processing, Pt 3, Proceedings*, 4234, 390–399.
- Iqbal, F., Lucieer, A., Barry, K., Wells, R., 2017. Poppy crop height and capsule volume estimation from a single UAS flight. *Remote Sens.* 9, 647.
- Jayathunga, S., Owari, T., Tsuyuki, S., 2018. Evaluating the performance of photogrammetric products using fixed-wing UAV imagery over a mixed conifer-broadleaf forest: comparison with airborne laser scanning. *Remote Sens.* 10, 187.
- Jin, X.L., Liu, S.Y., Baret, F., Hemerle, M., Comar, A., 2017. Estimates of plant density of wheat crops at emergence from very low altitude UAV imagery. *Remote Sens. Environ.* 198, 105–114.
- Johnston, K., Ver Hoef, J.M., Krivoruchko, K., Lucas, N., 2001. Using ArcGIS Geostatistical Analyst. Esri Redlands.
- Kachamba, D.J., Orka, H.O., Naesset, E., Eid, T., Gobakken, T., 2017. Influence of plot size on efficiency of biomass estimates in inventories of dry tropical forests assisted by photogrammetric data from an unmanned aircraft system. *Remote Sens.* 9.
- Kalacska, M., Chmura, G.L., Lukanus, O., Berube, D., Arroyo-Mora, J.P., 2017. Structure from motion will revolutionize analyses of tidal wetland landscapes. *Remote Sens. Environ.* 199, 14–24.
- Kataoka, T., Kaneko, T., Okamoto, H., Hata, S., 2003. Crop growth estimation system using machine vision. In: Advanced Intelligent Mechatronics, 2003. AIM 2003. Proceedings. 2003 IEEE/ASME International Conference on. IEEE, vol. 1072. pp. b1079–b1083.
- Kawashima, S., Nakatani, M., 1998. An algorithm for estimating chlorophyll content in leaves using a video camera. *Ann. Bot.* 81, 49–54.
- Kim, E., Lee, W.K., Yoon, M., Lee, J.Y., Son, Y., Abu Salim, K., 2016. Estimation of voxel-based above-ground biomass using airborne LiDAR data in an intact tropical rain forest, Brunei. *Forests* 7.
- Lati, R.N., Filin, S., Eisenberg, H., 2013a. Plant growth parameter estimation from sparse 3D reconstruction based on highly-textured feature points. *Precis. Agric.* 14, 586–605.
- Lati, R.N., Manevich, A., Filin, S., 2013b. Three-dimensional image-based modelling of linear features for plant biomass estimation. *Int. J. Remote Sens.* 34, 6135–6151.
- Leberl, F., Irschara, A., Pock, T., Meixner, P., Gruber, M., Scholz, S., Wiechert, A., 2010. Point Clouds: Lidar versus 3D Vision. *Photogramm. Eng. Remote Sens.* 76, 1123–1134.
- Li, W., Niu, Z., Chen, H.Y., Li, D., Wu, M.Q., Zhao, W., 2016. Remote estimation of canopy height and aboveground biomass of maize using high-resolution stereo images from a low-cost unmanned aerial vehicle system. *Ecol. Ind.* 67, 637–648.
- Li, W., Niu, Z., Huang, N., Wang, C., Gao, S., Wu, C.Y., 2015a. Airborne LiDAR technique for estimating biomass components of maize: a case study in Zhangye City, Northwest China. *Ecol. Ind.* 57, 486–496.
- Li, W., Niu, Z., Wang, C., Huang, W.J., Chen, H.Y., Gao, S., Li, D., Muhammad, S., 2015b. Combined use of airborne LiDAR and satellite GF-1 data to estimate leaf area index, height, and aboveground biomass of maize during peak growing season. *IEEE J. Sel. Top. Appl. Earth Obs. Remote Sens.* 8, 4489–4501.
- Louhaichi, M., Borman, M.M., Johnson, D.E., 2001. Spatially located platform and aerial photography for documentation of grazing impacts on wheat. *Geocarto Int.* 16, 65–70.
- Lowe, D.G., 1999. Object recognition from local scale-invariant features. In: Computer Vision, 1999. The Proceedings of the Seventh IEEE International Conference on. IEEE, pp. 1150–1157.
- Luo, S.Z., Wang, C., Xi, X.H., Pan, F.F., Peng, D.L., Zou, J., Nie, S., Qin, H.M., 2017. Fusion of airborne LiDAR data and hyperspectral imagery for aboveground and belowground forest biomass estimation. *Ecol. Ind.* 73, 378–387.
- Maimaitijiang, M., Ghulam, A., Sandoval, J.S.O., Maimaitiyiming, M., 2015. Drivers of land cover and land use changes in St. Louis metropolitan area over the past 40 years characterized by remote sensing and census population data. *Int. J. Appl. Earth Obs. Geoinf.* 35, 161–174.
- Maimaitijiang, M., Ghulam, A., Sidike, P., Hartling, S., Maimaitiyiming, M., Peterson, K., Shavers, E., Fishman, J., Peterson, J., Kadam, S., Burken, J., Fritsch, F., 2017. Unmanned Aerial System (UAS)-based phenotyping of soybean using multi-sensor data fusion and extreme learning machine. *ISPRS J. Photogramm. Remote Sens.* 134, 43–58.
- Malambo, L., Popescu, S., Murray, S., Putman, E., Pugh, N., Horne, D., Richardson, G., Sheridan, R., Rooney, W., Avant, R., 2018. Multitemporal field-based plant height estimation using 3D point clouds generated from small unmanned aerial systems high-resolution imagery. *Int. J. Appl. Earth Obs. Geoinf.* 64, 31–42.
- Mao, W., Wang, Y., Wang, Y., 2003. Real-time detection of between-row weeds using machine vision. In: 2003 ASAE Annual Meeting. American Society of Agricultural and Biological Engineers, p. 1.
- Marshall, M., Thenkabail, P., 2015. Advantage of hyperspectral EO-1 Hyperion over multispectral IKONOS, GeoEye-1, WorldView-2, Landsat ETM plus, and MODIS vegetation indices in crop biomass estimation. *ISPRS J. Photogramm. Remote Sens.* 108, 205–218.
- Nurminen, K., Karjalainen, M., Yu, X.W., Hyypä, J., Honkavaara, E., 2013. Performance of dense digital surface models based on image matching in the estimation of plot-level forest variables. *ISPRS J. Photogramm. Remote Sens.* 83, 104–115.
- Olsoy, P.J., Glenn, N.F., Clark, P.E., Derryberry, D.R., 2014. Aboveground total and green biomass of dryland shrub derived from terrestrial laser scanning. *ISPRS J. Photogramm. Remote Sens.* 88, 166–173.
- Patrick, A., Li, C.Y., 2017. High throughput phenotyping of blueberry bush morphological traits using unmanned aerial systems. *Remote Sens.* 9.
- Pottier, J., Jabot, F., 2017. Non-destructive biomass estimation of herbaceous plant individuals: a transferable method between contrasted environments. *Ecol. Ind.* 72, 769–776.
- Puliti, S., Orka, H.O., Gobakken, T., Naesset, E., 2015. Inventory of small forest areas using an unmanned aerial system. *Remote Sens.* 7, 9632–9654.
- Rahlf, J., Breidenbach, J., Solberg, S., Naesset, E., Astrup, R., 2014. Comparison of four types of 3D data for timber volume estimation. *Remote Sens. Environ.* 155, 325–333.
- Saberioon, M.M., Amin, M.S.M., Anuar, A.R., Gholizadeh, A., Wayayok, A., Khairunnizam Bejo, S., 2014. Assessment of rice leaf chlorophyll content using visible bands at different growth stages at both the leaf and canopy scale. *Int. J. Appl. Earth Obs. Geoinf.* 32, 35–45.
- Sagan, V., Maimaitijiang, M., Sidike, P., Ebilim, K., Peterson, K.T., Hartling, S., Esposito, F., Khanal, K., Newcomb, M., Pauli, D., 2019. UAV-Based High Resolution Thermal Imaging for Vegetation Monitoring, and Plant Phenotyping Using ICI 8640 P, FLIR Vue Pro R 640, and thermoMap Cameras. *Remote Sensing*, 11, 330.
- Schaefer, M.T., Lamb, D.W., 2016. A combination of plant NDVI and LiDAR measurements improve the estimation of pasture biomass in tall fescue (*Festuca arundinacea* var. Fletcher). *Remote Sens.* 8.
- Selkowitz, D.J., 2010. A comparison of multi-spectral, multi-angular, and multi-temporal remote sensing datasets for fractional shrub canopy mapping in Arctic Alaska. *Remote Sens. Environ.* 114, 1338–1352.
- Shao, Z.F., Zhang, L.J., 2016. Estimating forest aboveground biomass by combining optical and SAR data: a case study in Genhe, Inner Mongolia, China. *Sensors*, 16.
- Sidike, P., Sagan, V., Qumsiyeh, M., Maimaitijiang, M., Essa, A., Asari, V., 2018. Adaptive trigonometric transformation function with image contrast and color enhancement: application to unmanned aerial system imagery. *IEEE Geosci. Rem. Sens. Lett.*
- Stovall, A.E.L., Vorster, A.G., Anderson, R.S., Evangelista, P.H., Shugart, H.H., 2017. Non-destructive aboveground biomass estimation of coniferous trees using terrestrial LiDAR. *Remote Sens. Environ.* 200, 31–42.
- Swatantran, A., Dubayah, R., Roberts, D., Hofton, M., Blair, J.B., 2011. Mapping biomass and stress in the Sierra Nevada using lidar and hyperspectral data fusion. *Remote Sens. Environ.* 115, 2917–2930.
- Teillet, P.M., Barker, J.L., Markham, B.L., Irish, R.R., Fedosejevs, G., Storey, J.C., 2001. Radiometric cross-calibration of the Landsat-7 ETM+ and Landsat-5 TM sensors based on tandem data sets. *Remote Sens. Environ.* 78, 39–54.
- Tilly, N., Aasen, H., Bareth, G., 2015. Fusion of plant height and vegetation indices for the estimation of barley biomass. *Remote Sens.* 7, 11449–11480.
- Tilly, N., Hoffmeister, D., Cao, Q., Huang, S.Y., Lenz-Wiedemann, V., Miao, Y.X., Bareth, G., 2014. Multitemporal crop surface models: accurate plant height measurement and biomass estimation with terrestrial laser scanning in paddy rice. *J. Appl. Remote Sens.* 8.
- Tokola, T., Lofman, S., Erkkila, A., 1999. Relative calibration of multitemporal landsat data for forest cover change detection. *Remote Sens. Environ.* 68, 1–11.
- Torresan, C., Berton, A., Carotenuto, F., Di Gennaro, S.F., Gioli, B., Matese, A., Miglietta, F., Vagnoli, C., Zaldei, A., Wallace, L., 2017. Forestry applications of UAVs in Europe:

- a review. *Int. J. Remote Sens.* 38, 2427–2447.
- Tucker, C.J., 1979. Red and photographic infrared linear combinations for monitoring vegetation. *Remote Sens. Environ.* 8, 127–150.
- Turner, D., Lucieer, A., Wallace, L., 2014. Direct georeferencing of ultrahigh-resolution UAV imagery. *IEEE Trans. Geosci. Remote Sens.* 52, 2738–2745.
- Turner, D., Lucieer, A., Watson, C., 2012. An automated technique for generating georectified mosaics from ultra-high resolution unmanned aerial vehicle (UAV) imagery, based on structure from motion (SfM) point clouds. *Remote Sens.* 4, 1392–1410.
- Verma, N.K., Lamb, D.W., Reid, N., Wilson, B., 2016. Comparison of canopy volume measurements of scattered eucalypt farm trees derived from high spatial resolution imagery and LiDAR. *Remote Sens.* 8.
- Wallace, L., Hillman, S., Reinke, K., Hally, B., 2017. Non-destructive estimation of above-ground surface and near-surface biomass using 3D terrestrial remote sensing techniques. *METHODS ECOL. EVOL.* 8, 1607–1616.
- Walter, J., Edwards, J., McDonald, G., Kuchel, H., 2018. Photogrammetry for the estimation of wheat biomass and harvest index. *Field Crops Res.* 216, 165–174.
- Wang, C., Nie, S., Xi, X.H., Luo, S.Z., Sun, X.F., 2017. Estimating the biomass of maize with hyperspectral and LiDAR data. *Remote Sens.* 9.
- White, J.C., Wulder, M.A., Vastaranta, M., Coops, N.C., Pitt, D., Woods, M., 2013. The utility of image-based point clouds for forest inventory: a comparison with airborne laser scanning. *Forests* 4, 518–536.
- Woebbecke, D., Meyer, G., Von Bargen, K., Mortensen, D., 1992. Plant species identification, size, and enumeration using machine vision techniques on near-binary images [1836–20]. In: Proceedings-Spie the International Society for Optical Engineering. SPIE International Society For Optical, p. 208.
- Woebbecke, D.M., Meyer, G.E., Von Bargen, K., Mortensen, D., 1995. Color indices for weed identification under various soil, residue, and lighting conditions. *Trans. ASAE* 38, 259–269.
- Yang, G.J., Liu, J.G., Zhao, C.J., Li, Z.H., Huang, Y.B., Yu, H.Y., Xu, B., Yang, X.D., Zhu, D.M., Zhang, X.Y., Zhang, R.Y., Feng, H.K., Zhao, X.Q., Li, Z.H., Li, H.L., Yang, H., 2017. Unmanned aerial vehicle remote sensing for field-based crop phenotyping: current status and perspectives. *Front. Plant Sci.*, 8.
- Zeng, W.-S., 2015a. Integrated individual tree biomass simultaneous equations for two larch species in northeastern and northern China. *Scand. J. For. Res.* 30, 594–604.
- Zeng, W.-S., 2015b. Using nonlinear mixed model and dummy variable model approaches to develop origin-based individual tree biomass equations. *Trees* 29, 275–283.
- Zeng, W., Zhang, L., Chen, X., Cheng, Z., Ma, K., Li, Z., 2016. Construction of compatible and additive individual-tree biomass models for *Pinus tabulaeformis* in China. *Can. J. For. Res.* 47, 467–475.
- Zeng, W.S., Tang, S.Z., 2011. Bias correction in logarithmic regression and comparison with weighted regression for nonlinear models. *For. Res.* 24, 137–143.
- Zhao, K.G., Suarez, J.C., Garcia, M., Hu, T.X., Wang, C., Londo, A., 2018. Utility of multitemporal lidar for forest and carbon monitoring: tree growth, biomass dynamics, and carbon flux. *Remote Sens. Environ.* 204, 883–897.
- Zhao, P.P., Lu, D.S., Wang, G.X., Wu, C.P., Huang, Y.J., Yu, S.Q., 2016. Examining spectral reflectance saturation in landsat imagery and corresponding solutions to improve forest aboveground biomass estimation. *Remote Sens.* 8.
- Zhu, J., Huang, Z.H., Sun, H., Wang, G.X., 2017. Mapping forest ecosystem biomass density for Xiangjiang river basin by combining plot and remote sensing data and comparing spatial extrapolation methods. *Remote Sens.* 9.